IFT

Instituto de Física Teórica
Universidade Estadual Paulista

DISSERTAÇÃO DE MESTRADO IFT–M. 009/13

Estudo de Monte Carlo da Produção de Nova Ressonância Neutra Decaindo em Dois Bósons Vetoriais no Experimento CMS

José Cupertino Ruiz Vargas

Orientador

Prof. Sérgio F. Novaes

Co–orientador

Dr. Thiago R. F. P. Tomei

Fevereiro 2013

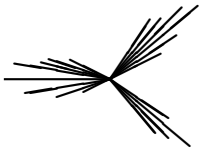

Instituto de Física Teórica
Universidade Estadual Paulista

MASTER DISSERTATION IFT–M. 009/13

Monte Carlo Study of New Neutral Resonance Production in a Diboson Channel at the CMS Experiment

José Cupertino Ruiz Vargas

Advisor

Prof. Sérgio F. Novaes

Co–advisor

Dr. Thiago R. F. P. Tomei

February 2013

Acknowledgements

I would like to thank my supervisor Prof. Sérgio Novaes, for his dedication, patience, and for introducing me to the CMS Collaboration.
I would also like to thank my family: father, mother and brothers, for their encouragement and especially because they always have trusted me.
I would like to thank all SPRACE staff. Thiago, Flavia, Pedro, Cesar and Angelo, for their expertise and continuous support.
I would like to thank my friends at IFT. In particular David, Prieslei and Ricardo, for their camaraderie.
Finally, I would like to thank CAPES funding agency for the financial support.

Resumo

Estudamos neste trabalho a produção de um novo bóson vetorial neutro pelo detector *Compact Muon Solenoid* (CMS) do *Large Hadron Collider* (LHC). Adotamos as condições de operação do LHC em 2012, *i.e.* energia do centro de massa de 8 TeV e luminosidade integrada de 20 fb^{-1}.

Nós realizamos um estudo de viabilidade da busca de física além do modelo padrão através da produção e decaimento de uma ressonância exótica em um par de bósons vetoriais W^+W^-. O fundo do Modelo Padrão foi estimado por amostras de Monte Carlo geradas centralmente pela colaboração CMS, enquanto as amostras do sinal foram simuladas localmente por nós no SPRACE. A massa transversal invariante foi reconstruída usando léptons de cargas opostas mais a energia transversal faltante.

Uma análise da significância, considerando sinais com massas de 0.5, 1, 1.5, e 2 TeV, foi implementada para melhorar a eficiência da seleção de eventos. Finalmente, para avaliar a sensibilidade da análise, foram estabelecidos limites esperados com 95% CL para a seção de choque multiplicada pela razão de ramificação $\sigma(pp \to Z') \times BR(Z' \to WW \to e + \mu + \not{E}_{\text{T}})$.

Palavras Chaves: Física de Altas Energias; Física de Partículas; Colisores Hadrônicos; Física Além do Modelo Padrão.

Áreas do conhecimento: Física de Altas Energias.

Abstract

In this work, we study the production of a new neutral vector boson at the *Compact Muon Solenoid* (CMS) detector from the *Large Hadron Collider* (LHC). We adopt the operation parameters of the LHC during the 2012 run, *i.e.* center-of-mass energy of 8 TeV and integrated luminosity of 20 fb $^{-1}$.

We conducted a feasibility study of the search for physics beyond the standard model through the production and decay of an exotic resonance in a pair of vector bosons W^+W^-. The Standard Model background was estimated by Monte Carlo samples centrally generated by CMS, while the signal samples were simulated locally by us at SPRACE. The invariant transverse mass was reconstructed using the oppositely charged leptons and the missing transverse energy.

An analysis of the significance of the signal, considering resonances with mass of 0.5, 1, 1.5, and 2 TeV, was implemented to improve the efficiency of the event selection. Finally, to assess the sensitivity of the analysis, we calculated the 95% CL limits for the cross section times the branching ratio, $\sigma(pp \to Z') \times BR(Z' \to WW \to e + \mu + \not{E}_{\mathrm{T}})$.

Key Words: High Energy Physics; Particle Physics; Hadronic Colliders, Physics Beyond the Standard Model.

Research area: High Energy Physics.

Contents

List of Tables

List of Figures

Chapter 1

Introduction

Understanding nature from the study of its microscopic constituents is the goal of Particle Physics. The knowledge about elementary particles obtained through decades of experimental discoveries, accompanied by theoretical and technological developments, allowed to establish the Standard Model (SM) as the main theory of Particle Physics. The model embeds two quantum field theories, quantum chromodynamics for strong interactions and the Weinberg-Salam theory for weak and electromagnetic interactions.

The Quantum Electrodynamics (QED), which describes the electromagnetic interaction with an astonishing precision, turned into a prototype gauge theory for the other interactions. After the discovery of the asymptotic freedom of the non-abelian gauge theories, a reliable theory for the strong interactions at short distance became possible. Based on the $SU(3)_C$ colour group, the Quantum Chromodynamics (QCD) was very successful describing the strong phenomena at high energies.

The weak force has a significant influence only to a distance of a hundredth the radius of a proton, and its short range implies that the virtual particles exchanged in weak interactions must be very massive. In fact, the weak bosons ($W^{\pm}$, Z^0) are around ninety times heavier than a proton. In 1967 Abdus Salam and Steven Weinberg proposed a model of the weak interaction in which the gauge bosons acquire mass through the Higgs mechanism. They explored the same gauge group proposed in 1961 by Sheldon Glashow, the $SU(2)_L \times U(1)_Y$. In order to preserve local symmetries, four gauge bosons are introduced at the outset all of them massless.

The spontaneous symmetry breaking is implemented by a potential constructed out of a Higgs complex scalar doublet, represented by four scalar particles. Three of the Higgs fields are absorbed by the gauge bosons W^+, W^- and Z^0. The fourth gauge boson remains massless, being associated with the photon, the mediator

of the electromagnetic interaction. The three scalar particles that lend mass to the gauge bosons disappear from the physical spectrum, but one neutral scalar, the Higgs particle, is not absorbed and should be observed in experiments.

The first decisive test of the electroweak model was the existence of weak interaction between neutral currents represented by the exchange of the Z^0, observed in 1973 at CERN. Without the Z^0 contribution, any weak interaction would necessarily entail an exchange of electric charge by the $W^{\pm}$ bosons. However, particles interacting through neutral weak currents keep their original identities. The absence of flavor-changing neutral currents is a prominent feature of the electroweak theory.

During the 80's both W and Z bosons were produced on-shell at the $Sp\bar{p}S$ collider at CERN. In the next decade, the four collaborations of the Large Electron-Positron Collider (LEP) were able to deeply scrutinise several aspects of the standard model. They measured almost 20 parameters related to the SM and arrived to an impressive agreement between experimental data and theoretical predictions.

Another intriguing prediction of the SM is the Higgs boson, whose mass is not predicted by the theory. After 45 years of intensive search for this particle, in 2012, both CMS and Atlas collaborations of LHC have presented very strong evidences that the Higgs boson has been discovered. A boson with mass around 125 GeV sharing much of the characteristics of the Higgs has showed up mainly in the $\gamma\gamma$ and four leptons final states.

Despite its great success describing all the experimental data at present, the SM has some intrinsic problems. For instance, the SM does not predict the value of the masses of the elementary particle and does not furnish an explanation for the huge amplitude of the mass spectrum. The SM contains a large number of parameters, does not explain the generation structure, and has difficulties associated with hierarchy and fine-tuning problems. It does not incorporate gravity and fails to unify the electroweak and strong forces. The SM does not have any candidate that could explain the existence of the dark matter either.

Soon after the proposal of the electroweak model there were many suggestions for extended or alternative electroweak gauge theories, some of which involved new heavy gauge bosons, electrically neutral and quite similar to Z^0 bosons.

We shall call "Z prime" (Z') any neutral spin–1 resonance more massive than the Z^0 of the SM. This particle could be observed in Drell-Yan production followed

by its decay, for instance, into a lepton-antilepton pair. On the other hand, scenarios presenting extra dimensions allow Z' resonances to emerge as Kaluza-Klein excitations of the Z^0 boson. Such models, motivated as alternatives to the elementary Higgs for electroweak symmetry breaking, may involve fermiophobic Z' that can be produced in proton-proton collisions and detected by their coupling to standard $W^{\pm}$ bosons.

A diboson W^+W^- can decay into a fully leptonic, semileptonic, or fully hadronic channel. In the first mode, it is possible to obtain a quite clean spectrum of the transverse mass, thus any deviation from SM predictions would indicate new physics. For decades, direct searches for exotic resonances decaying into dibosons have been performed without any evidence of physics beyond the SM so far.

The experimental discovery of a new Z' would be exciting, but the implications would be much greater than just the existence of a new vector boson. Breaking the $U(1)'$ symmetry would require an extended Higgs sector, with significant consequences for collider physics and cosmology such as dark matter, electroweak baryogenesis, etc. In some constructions, especially in the ones string derived, the $U(1)'$ charges do not present a family universality, which can lead to flavour changing neutral current effects. The decays of a heavy Z' may be a useful production mechanism for exotics and superpartners. Finally, the constraints from the $U(1)'$ symmetry can significantly alter the theoretical possibilities for neutrino mass.

This present study is based on a simulation of the process,

$$pp \to Z' \to W^+W^- \to \ell^+\nu_\ell\,\ell'^-\nu_{\ell'} \tag{1.1}$$

where ℓ stands for lepton, muon or electron, and ν_ℓ the respective neutrino. We choose a particular Z' model to simulate the signatures of this signal upon a SM background. We have taken into account the parameters of the 2012 operation of LHC, considering a center-of-mass energy of $\sqrt{s} = 8$ TeV and an integrated luminosity $L = 20\,\text{fb}^{-1}$.

In the next Chapter, we present a synthetic review of the SM, *i.e.* quantum chromodynamics and the electroweak theory. Some aspects of the possible physics beyond the SM and motivations for exotic searches are presented in Chapter 3. Chapter 4 gives a fast overview of the LHC and outlines the CMS experiment,

presenting aspects on particle identification, software and computing. Chapter 5 contains the core of our analysis, where the study of the above channel is fully addressed. Finally, a brief summary of the work and its conclusions are given in chapter 6.

Chapter 2

The Standard Model

Four basic forces mediate all known interactions among the particles of matter. Electromagnetism and gravitation are infinite range forces, so they are familiar to everyone for their macroscopic effects. The two remaining forces, which are called the weak force and the strong force, cannot be perceived directly because their influence extends no larger than the radius of an atomic nucleus. The strong force binds together the protons and neutrons in the nucleus, and sticks the quarks to constitute hadrons. The weak force is mainly responsible for decay processes, characterised by a short lifetime due to the large mass of the weak bosons that carry the interaction.

The Standard Model (SM) [1,3,4] is a field theory that incorporates quantum mechanics and special relativity to describe three of the four fundamental interactions: strong, electromagnetic, and weak interactions. The fourth fundamental interaction, gravity, is far weaker and is not expected to contribute significantly to the physical processes involved in a collision between elementary particles.

According to the SM, there exist 12 fermions (6 quarks plus 6 leptons), 4 vector bosons (W, Z, photon, gluon), and one scalar field (Higgs) responsible for the mechanism of electroweak symmetry breaking (EWSB). Each particle has its own anti-particle related by charge conjugation.

The quarks are the constituents of composite particles and can combine to form hadrons which are bound states of 2 (mesons) or 3 (barions) quarks. Quarks cannot be observed as free particles, have fractional electric charge, and a quantum number called "colour" which is the source of the strong interaction. Gluons, the mediators of colour flow in the strong interactions, carry colour and anti-colour.

The leptons, having the electron as the best known member, do not undergo strong interactions because they do not carry colour. There exist two classes of leptons: charged leptons, and neutral leptons better known as neutrinos. Neutrinos rarely interact with anything, and their detection is usually inferred by energy

imbalance.

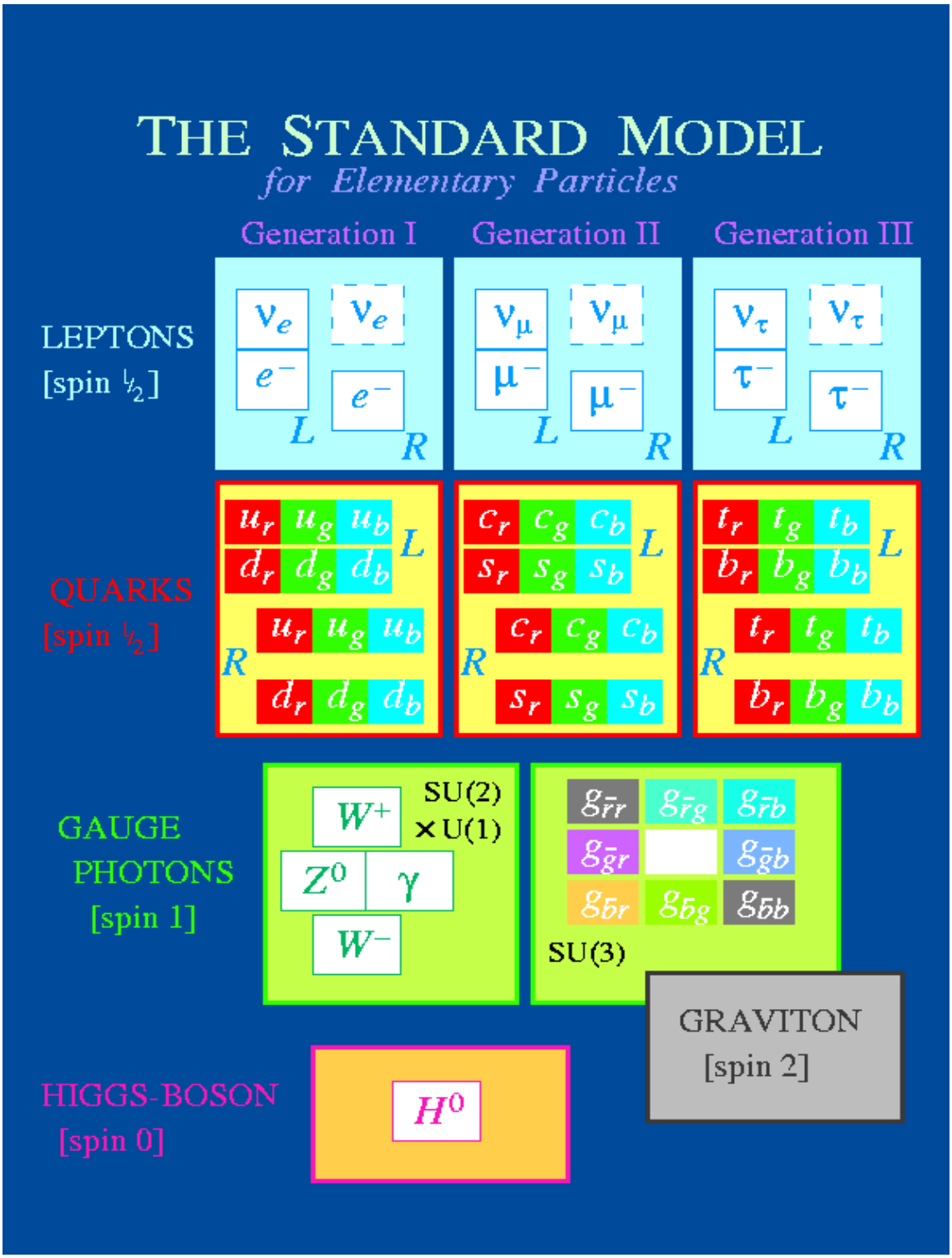

Figure 2.1: Arrangements of the most elementary particles in the standard model. (L)Left and (R)Right helicities of the spin 1/2 particles are arranged differently [2].

2.1 Structure of the SM

The fundamental particles of matter are six leptons and six flavours of quarks (Fig. 2.1), each of the quarks being present in three colours. The SM of elementary particle interactions describes the forces of nature by means of non-Abelian gauge theories. Electromagnetism and weak force are mediated by the gauge particles of the Glashow–Weinberg–Salam model, namely the massless photon and a triplet of massive vector bosons, the W^+, W^-, and Z^0. The strong force is attributed to the eight massless gluons of quantum chromodynamics. In additions there is one Higgs boson, which is massive and electrically neutral.

The fields associated with the elementary particles are representations of a symmetry group. For the SM, the governing symmetry group is

$$SU(3)_C \times SU(2)_L \times U(1)_Y \,. \tag{2.1}$$

The factor $SU(3)_C$ corresponds to the strong sector, carries the colour charge, and generates $(3^2 - 1)$ gauge fields associated with the eight gluons. The factor $SU(2)_L \times U(1)_Y$ corresponds to the electroweak sector, carries iso-spin and hypercharge, and generates $(3 + 1)$ gauge fields associated with the weak bosons and the photon.

2.1.1 Strong Sector

Quantum Chromodynamics (QCD) is the theory of the strong interactions between quarks and gluons, governed by the symmetry group $SU(3)_C$. The fundamental representation of $SU(3)_C$ is a triplet, so the three quark colours red, green, and blue, or (r, g, b), form the fundamental representation:

$$q \doteq \begin{pmatrix} q^r \\ q^g \\ q^b \end{pmatrix} . \tag{2.2}$$

In this representation, the $SU(3)_C$ generators are the Gell-Mann matrices denoted λ^a, with $a = 1, \ldots, 8$. The QCD Lagrangian is given by

$$\mathscr{L}_{QCD} = \sum_{q=u,d,s\ldots} \bar{q}(i \not{D} - m_q)q \; - \; \frac{1}{4} G^a_{\mu\nu} G^{a\mu\nu} \tag{2.3}$$

where

$$G^a_{\mu\nu} \equiv \partial_\mu G^a_\nu - \partial_\nu G^a_\mu - g_s f^{abc} G^b_\mu G^c_\nu$$

is the strength tensor of the gluon field G^a_μ. The structure constant f^{abc} is defined through

$$[\lambda^a, \lambda^b] = 2if^{abc}\lambda^c \ .$$

The sum in Eq. 2.3 runs over the quark flavours up, down, strange, charm, bottom, and top. The covariant derivate is defined as

$$D_\mu q \equiv \left(\partial_\mu + ig_s \frac{\lambda^a}{2} G^a_\mu\right) q \tag{2.4}$$

where g_s is the coupling of the strong force.

The strong interactions have a characteristic energy scale $\Lambda \sim 200$ MeV interpreted as the energy at which the coupling constant diverges. The running of the coupling constant obtained by the renormalization group equation, at leading order of perturbation theory is given by

$$\alpha_S(Q^2) = \frac{12\pi}{(33 - 2n_f)\log(Q^2/\Lambda^2)} \tag{2.5}$$

where n_f is the number of quark flavours and Q^2 the probed energy. At very large Q^2 (corresponding to small distances), α_S becomes increasingly small. This phenomena is known as asymptotic freedom, property that allows perturbative expansion at small distances.

2.1.2 Electroweak Sector

The 12 fundamental fermions are grouped in three generations:

$$\begin{Bmatrix} \nu_e & u \\ e & d \end{Bmatrix}, \quad \begin{Bmatrix} \nu_\mu & c \\ \mu & s \end{Bmatrix}, \quad \begin{Bmatrix} \nu_\tau & t \\ \tau & b \end{Bmatrix}$$

The three generations differ only in the mass and the flavour quantum number, but are representations of the same symmetry group. Each generation is separated in two doublets and three singlets of $SU(2)_L$. For the first generation we have

$$\begin{Bmatrix} \nu_e & u \\ e & d \end{Bmatrix} \equiv \begin{pmatrix} \nu_e \\ e \end{pmatrix}_L, \begin{pmatrix} u \\ d \end{pmatrix}_L, e_R, u_R, d_R$$

Generation			$SU(2)_L$	$U(1)_Y$
I	II	III		
$\binom{u}{d}_L$	$\binom{c}{s}_L$	$\binom{t}{b}_L$	doublet	$+\frac{1}{6}$
u_R	c_R	t_R	singlet	$+\frac{2}{3}$
d_R	s_R	b_R	singlet	$-\frac{1}{3}$
$\binom{\nu_e}{e}_L$	$\binom{\nu_\mu}{\mu}_L$	$\binom{\nu_\tau}{\tau}_L$	doublet	$-\frac{1}{2}$
e_R	μ_R	τ_R	singlet	-1

Table 2.1: Fermion fields, representation and corresponding hypercharge.

and similarly for the other two generations.

The subscripts L and R stand for left and right chiral component. For a Dirac spinor f its chiral decomposition is

$$f = f_L + f_R = P_L f + P_R f \tag{2.6}$$

where $P_{L,R} = (1 \mp \gamma_5)/2$ are the left and right chiral projectors. Left and right fields belong to different representations of $SU(2)$ and exhibit different values of $U(1)_Y$ hypercharge, property summarize in Table 2.1.

Using the notation

$$\psi_1 = \begin{pmatrix} u \\ d \end{pmatrix}_L \ , \ \psi_2 = u_R \ , \ \psi_3 = d_R \tag{2.7}$$

the Lagrangian for fermions* can be written

$$\mathscr{L}_{\text{fermion}} = \sum_{j=1}^{3} i\bar{\psi}_j \gamma^\mu D_\mu \psi_j \tag{2.8}$$

*We only consider quarks in the first generation to derive the charge current, though the result can be generalized to include more generations and leptons as well.

with the covariant derivates defined as

$$\begin{aligned} D_\mu \psi_1 &\equiv \left[\partial_\mu + ig\frac{\sigma_i}{2}W_\mu^i + ig' y_1 B_\mu\right]\psi_1 \\ D_\mu \psi_2 &\equiv \left[\partial_\mu + ig' y_2 B_\mu\right]\psi_2 \\ D_\mu \psi_3 &\equiv \left[\partial_\mu + ig' y_3 B_\mu\right]\psi_3 \,. \end{aligned}$$

g and g' are the $SU(2)_L$ and $U(1)_Y$ gauge couplings, W_μ^i and B_μ are the respective gauge bosons, y_j are the hypercharges, and σ^i the Pauli matrices.

The charge current Lagrangian obtained from 2.8 corresponds to

$$\begin{aligned} -\mathscr{L}_{\mathrm{CC}} &= g\bar{\psi}_1\gamma^\mu\frac{\sigma^1}{2}W_\mu^1\psi_1 + g\bar{\psi}_1\gamma^\mu\frac{\sigma^2}{2}W_\mu^2\psi_1 \\ &= \frac{g}{\sqrt{2}}\left\{\bar{u}_L\gamma^\mu d_L W_\mu^+ + \bar{d}_L\gamma^\mu u_L W_\mu^-\right\} \end{aligned} \tag{2.9}$$

where

$$W_\mu^\pm = (W_\mu^1 \mp iW_\mu^2)/\sqrt{2}\,.$$

The neutral current Lagrangian is given by

$$-\mathscr{L}_{\mathrm{NC}} = gJ_3^\mu W_\mu^3 + g' J_Y^\mu B_\mu = eJ_{em}^\mu A_\mu + g_1 J_1^\mu Z_{1\mu}^0\,. \tag{2.10}$$

The currents J_3^μ and J_Y^μ are

$$J_3^\mu = \sum_f \bar{f}\gamma^\mu[t_{f_L}^3 P_L + t_{f_R}^3 P_R]f \tag{2.11}$$

$$J_Y^\mu = \sum_f \bar{f}\gamma^\mu[y_{f_L} P_L + y_{f_R} P_R]f \tag{2.12}$$

where $t_{f_L}^3$ ($t_{f_R}^3$) is the third component of weak isospin for the left (right) chiral component of fermion f. For quarks in the first generation,

$$t_{u_L}^3 = +\tfrac{1}{2}\,, \qquad t_{d_L}^3 = -\tfrac{1}{2}\,, \qquad \text{and} \qquad t_{u_R}^3 = t_{d_R}^3 = 0. \tag{2.13}$$

The weak hypercharges $y_{f_{L,R}}$ are chosen to yield the correct electric charges,

$$t_{f_L}^3 + y_{f_L} = t_{f_R}^3 + y_{f_R} = q_f \tag{2.14}$$

where q_f is the electric charge of f in units of the positron charge.

The mass eigenstates in Eq. 2.10 are the massless photon A_μ and the massive $Z^0_{1\mu} \equiv Z_\mu$, where

$$A_\mu = \sin\theta_W W^3_\mu + \cos\theta_W B_\mu \tag{2.15}$$

$$Z_\mu = \cos\theta_W W^3_\mu - \sin\theta_W B_\mu \tag{2.16}$$

and the weak angle is $\theta_W \equiv \tan^{-1}(g/g')$. The new gauge couplings are

$$e \equiv g\sin\theta_W\,, \qquad g_1^2 \equiv g^2 + g'^2 = g^2/\cos\theta_W\,. \tag{2.17}$$

The currents in the new basis are

$$J^\mu_{em} = \sum_f q_f \bar{f}\gamma^\mu f \tag{2.18}$$

$$J^\mu_1 = \sum_f \bar{f}\gamma^\mu[\epsilon^1_L(f)P_L + \epsilon^1_R(f)P_R]f \tag{2.19}$$

with the chiral couplings

$$\epsilon^1_L(f) = t^3_{f_L} - q_f\sin^2\theta_W\,, \qquad \epsilon^1_R(f) = t^3_{f_R} - q_f\sin^2\theta_W\,. \tag{2.20}$$

2.1.3 The Higgs Mechanism

The weak bosons of the SM acquire mass through a spontaneous symmetry breaking in which 3 of the 4 generator of the electroweak sector are broken

$$SU(2)_L \times U(1)_Y \to U(1)_{EM}\,.$$

To illustrate the mechanism, consider the gauge group $G = SU(N)$, with $N-1$ diagonal generators. G can be broken by the vacuum expectation value (VEV) of a real adjoint Higgs representation Φ, which can be represented by a Hermitian traceless $N \times N$ matrix

$$\Phi = \sum_{i=1}^{N^2-1} \varphi^i T_i \tag{2.21}$$

where φ^i are the real components of Φ and the T_i are the fundamental $(N \times N)$ representation matrices. When Φ acquires a VEV, $\langle\Phi\rangle$, G is broken to a subgroup associated with those generators which commute with $\langle\Phi\rangle$. The VEV $\langle\Phi\rangle$ can be diagonalized by an $SU(N)$ transformation, so that the $N-1$ diagonal generators

remain unbroken.

The SM involves a scalar Higgs doublet

$$\phi = \begin{pmatrix} \phi^+ \\ \phi^0 \end{pmatrix} \tag{2.22}$$

through the scalar Lagrangian

$$\mathscr{L}_{\text{scalar}} = (D^\mu \phi)^\dagger D_\mu \phi - \mu^2 \phi^\dagger \phi - h(\phi^\dagger \phi)^2 \quad , \quad (\mu^2 < 0 < h) \tag{2.23}$$

with the covariant derivate given by

$$D_\mu \phi = \left(\partial_\mu + igW_\mu^i \frac{\sigma^i}{2} + ig' y_\phi B_\mu\right)\phi \,. \tag{2.24}$$

The neutral component ϕ^0 has weak isospin and weak hypercharge

$$t_{\phi^0} = -t_{3\phi^0} = y_{\phi^0} = \tfrac{1}{2} \tag{2.25}$$

where t_3 is the third component of weak isospin, $y_i = q_i - t_{3i}$ the weak hypercharge. When the neutral scalar field ϕ^0 accquire a VEV, the photon A_μ (Eq. 2.15) remain massless, while the Z_μ field develops a mass term

$$M_{Z^0}^2 \equiv \frac{1}{2} g^2 \left|\langle \phi^0 \rangle\right|^2 = \frac{1}{4} g^2 v^2 = \frac{M_W^2}{\cos^2 \theta_W} \tag{2.26}$$

where

$$v^2 = 2\left|\langle \phi^0 \rangle\right|^2 \sim \left(\sqrt{2} G_F\right)^{-1} \sim (246\,\text{GeV})^2 \tag{2.27}$$

is the square of the weak scale and G_F is the Fermi constant.

The Higgs field also enters in the Yukawa Lagrangian (ignoring family indices)

$$-\mathscr{L}_{Yuk} = h_d \bar{Q}_L \phi d_R + h_u \bar{Q}_L \tilde{\phi} u_R + h_e \bar{L}_L \phi e_R + h.c. \tag{2.28}$$

where $Q_L \equiv \binom{u_L}{d_L}$, $L_L \equiv \binom{\nu_L}{e_L}$. h_d, h_u, and h_e are the Yukawa constants which are directly related with the mass of the fermions. The tilde field is defined by

$$\tilde{\phi} \equiv i\sigma^2 \phi^* = \begin{pmatrix} \phi^{0*} \\ -\phi^- \end{pmatrix} \tag{2.29}$$

where σ^2 is the second Pauli matrix. After the spontaneous symmetry breaking the mass of the fermions springs

$$-\mathscr{L}_{Yuk} = \frac{1}{\sqrt{2}}(v+H)(h_d\bar{d}d + h_u\bar{u}u + h_e\bar{e}e) \tag{2.30}$$

where H is the scalar field of the Higgs remaining.

A single Higgs doublet suffices for the SM, but in many extensions including some $U(1)'$ models, a second doublet may be introduced.

Fine-tunning on the Higgs mass

One important issue is associated with the radiative corrections to the Higgs boson mass represented by the loop diagrams depicted in Fig. 2.2.

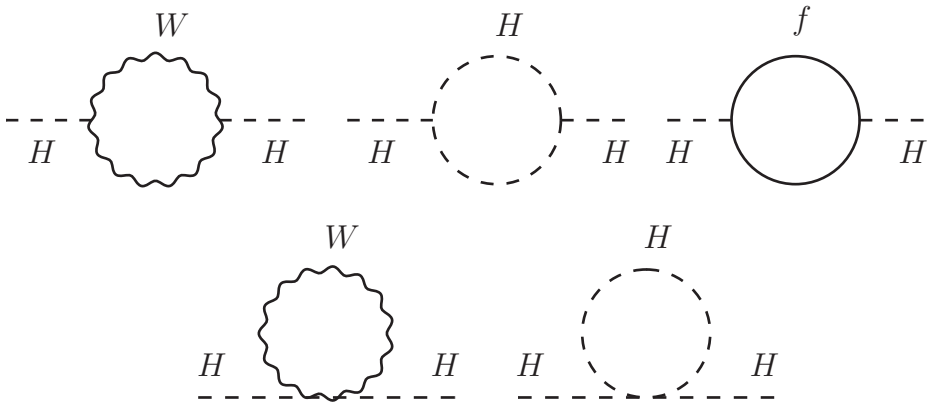

Figure 2.2: Radiative corrections to the Higgs mass.

The Higgs mass receive quantum corrections from loops that contain bosons (W, Z, Higgs) and fermions, with the last one being dominated by the top quark since its contribution goes with the square of the fermion mass. Taking into account those contributions we can write the renormalised Higgs mass as, [6]

$$\underbrace{M_H^2}_{\text{physical}} = \underbrace{M_{0,H}^2}_{\text{bare}} + \underbrace{\Lambda^2\left[6M_W^2 + 3M_Z^2 + M_H^2 - 12M_{\text{top}}^2\right]\frac{G_F}{4\pi^2\sqrt{2}}}_{\text{loop corrections}} \tag{2.31}$$

where Λ is the maximum energy for which the SM applies, or in other words, for energies larger than Λ a new theory should be taken into account. In principle, this scale can be as large as the Plank scale , that is,

$$\Lambda \sim M_{\text{Planck}} = (\hbar c/G_{\text{Newton}})^{1/2} \approx 1.2 \times 10^{19}\,\text{GeV}\,.$$

According to Eq. 2.31, the quantum correction goes with Λ^2 and it contains the sum of the effect of the bosons loops minus the sum of the effect of the fermions loop. It is important to notice that the quantum correction is not proportional to the Higgs mass itself. Therefore, the correction is present even for a Higgs with zero bare mass.

The physical Higgs mass is equal to the bare mass plus a very large number (Λ^2) multiplied by a (negative) loop factor. Therefore, in order to obtain a reasonable value for the physical Higgs mass (let us say, 125 GeV) one must have a very fine-tuning cancellation between the radiative correction and the bare mass. Even when the scale is not extremely large ($\Lambda \simeq 5$ TeV), a careful balancing is required to maintain a small Higgs mass (Fig 2.3).

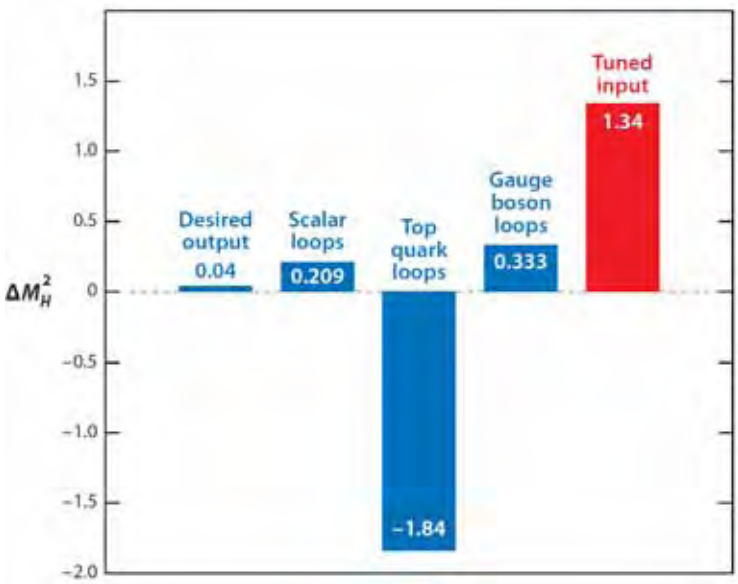

Figure 2.3: Relative contributions to ΔM_H^2 for a value of $\Lambda = 5$ TeV [6].

Unless we suppose that the bare mass and the quantum corrections are finely tuned to yield $M_H \sim 125$ GeV, some new physics must intervene. Such precise balancing is utterly unnatural in physics theories, leading the physicists to propose a series of ways in which this cancellation could occur naturally. For instance, supersymmetry [7] exploits the fact that fermion loops contribute with an overall minus sign relative to the boson loops (because of Fermi statistics), balancing the contributions of fermion and boson loops. In unbroken supersymmetry, the masses of bosons are degenerate with those of their fermion counterparts, so the cancellation is exact.

Chapter 3

Going Beyond the Standard Model

3.1 Exploring the TeV Scale

The standard model is in very good agreement with all experimental data obtained so far. Despite this great success, it is believed that the SM is inadequate since it contains a large number of parameters and it has too many features which are put by hand. The SM does not explain the generation structure, and it does not make specific predictions for the masses of the quarks and leptons. The SM leaves unexplained how the Higgs boson could have a light mass (around 125 GeV) in the face of quantum corrections that tend to lift it toward the Plank scale. Other questions that lie beyond the scope of the SM are related to the nature of dark matter, the matter asymmetry of the universe, the quantization of electric charge, and the role of gravity. Those fundamental topics have motivated theoreticians and phenomenologists to construct extensions to the SM.

Several proposals for the so-called physics beyond the standard model (BSM) [8] have been proposed with the motivation of solving the fine-tuning associated with the quadratic divergence in the Higgs mass [9]. These involve, for instance, the supersymmetric models (SUSY) [7] and various forms of dynamical symmetry breaking and little Higgs models [10]. Some versions of theories with large extra dimensions [11], which allow the W/Z bosons to propagate freely in the extra dimensions, give rise to Kaluza-Klein [12] excitations. Such excitations can also occur, for instance, in Randall-Sundrum models [13] and have motivated several experimental searches [14–17].

Another especial motivation came from the desire to have a grand unified theory (GUT) [18], which could unify the strong and electroweak interactions within the context of a single gauge group. The simplest GUT is based on the SU(5) group [19], however it still requires a large number of a priori unknown parameters and fails to deal with most of the theoretical difficulties of the SM. In

addition, the predictions of SU(5) model are inconsistent with data on both the proton lifetime and the electroweak mixing angle ($\sin^2\theta$). The failures of the SU(5) have led to the examination of larger GUT groups such as SO(10) [20], the next simplest Lie group that is able to accommodate the SM group structure. In SO(10), the three copies of the generation structure are still put in by hand. Theories based on E_6 [21] are the next natural choice after SO(10). In those E_6 models, the SM structure is extended to include a product of $U(1)_\psi \times U(1)_\chi$.

In this work, we are interested in exploring the physics beyond the standard model at the TeV scale, well within the LHC reach. The so-called Exotica area encompasses in the CMS Collaboration all BSM models which are not based on minimal SUSY model or its extensions. A non-exhaustive list includes the searches for heavy resonances, composite objects, 4th generation quarks, long-lived particles, leptoquarks, black holes, etc.

After the shut down of the Tevatron collider at Fermilab [22], the CERN LHC collider is the hadron collider at the energy forefront. A summary of the CMS exotic searches is presented in Fig. 3.1, which shows the mass limits at 95% CL for different searches. So far, no clear sign of exotic phenomena has been identified, neither by CMS [23] and ATLAS [24] nor by the experiments making precision measurements. However the search for new physics phenomena is the most important item of the LHC agenda during the next more than 20 years of scheduled operation.

3.2 Extended U(1)′ Model: An Example

A quite natural extension to the standard model is to broaden the gauge structure of the model by adding, for instance, one or more $U(1)'$ groups. As pointed out by Langacker in reference [5], the extension to a gauge group

$$SU(2) \times U(1)_Y \times U(1)'^n, \qquad n \geq 1 \tag{3.1}$$

requires a generalisation of the neutral current (Eq. 2.10)

$$-\mathscr{L}_{\mathrm{NC}} = eJ^\mu_{em}A_\mu + \sum_{\alpha=1}^{n+1} g_\alpha J^\mu_\alpha Z^0_{\alpha\mu} \tag{3.2}$$

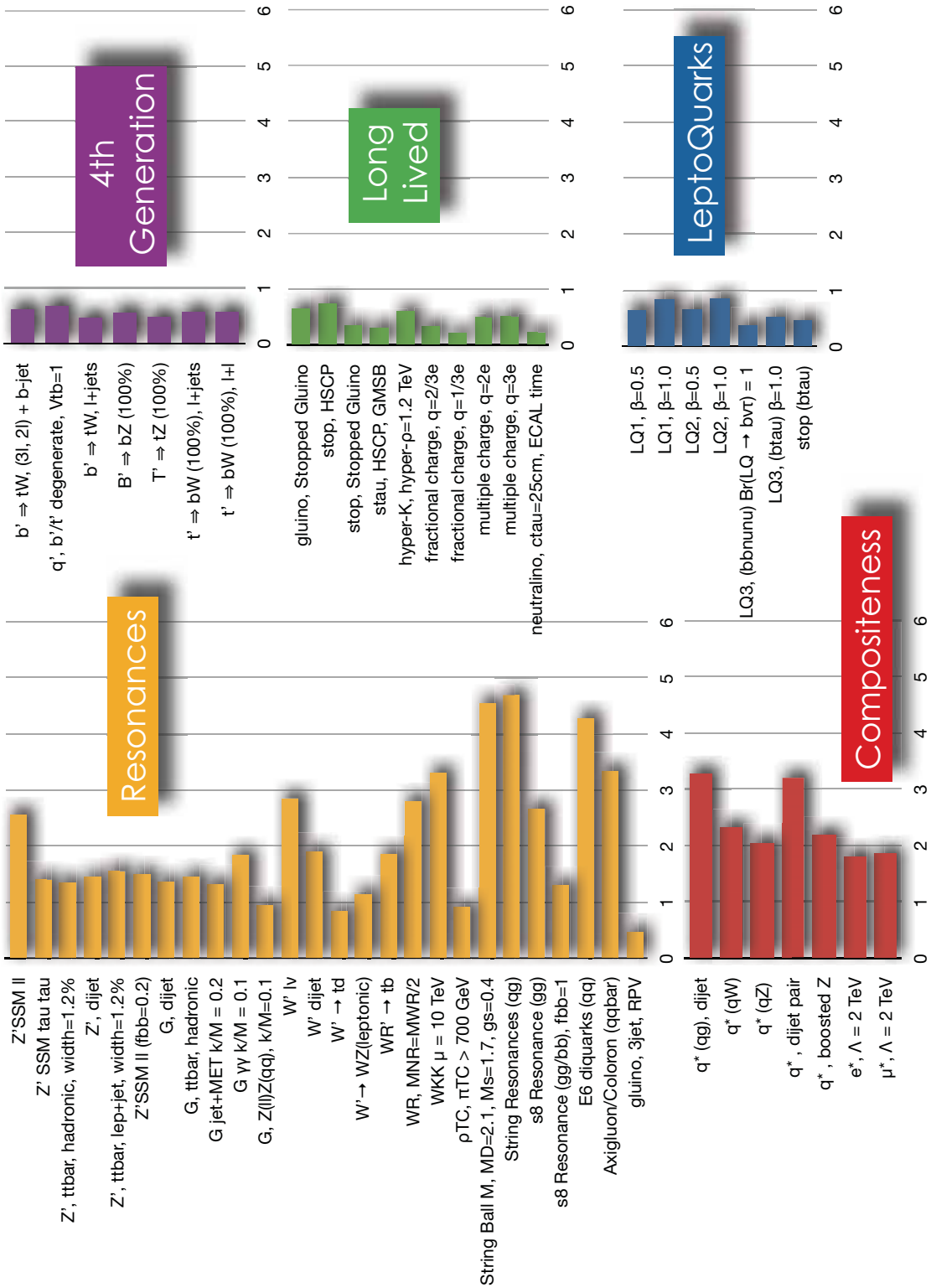

Figure 3.1: Summary of mass limits (TeV) in CMS exotica searches [23].

where g_1, $Z^0_{1\mu}$, and J^μ_1 are respectively the gauge coupling, gauge boson, and the neutral current of the SM. Similarly, g_α and $Z^0_{\alpha\mu}$, $\alpha = 2 \cdots n+1$, are the gauge couplings and gauge bosons for the additional $U(1)'$ groups.

The currents in Eq. 3.2 can be written as,

$$\begin{aligned} J^\mu_\alpha &= \sum_f \bar{f}\gamma^\mu \left[\epsilon^\alpha_L(f)P_L + \epsilon^\alpha_R(f)P_R\right] f \\ &= \tfrac{1}{2}\sum_f \bar{f}\gamma^\mu \left[g^\alpha_V(f) - g^\alpha_A(f)\gamma^5\right] f\,. \end{aligned} \tag{3.3}$$

The chiral couplings $\epsilon^\alpha_{L,R}(f)$ are respectively the $U(1)_\alpha$ charges for the left and right components of fermion f, and

$$g^\alpha_{V,A}(f) = \epsilon^\alpha_L(f) \pm \epsilon^\alpha_R(f) \tag{3.4}$$

are the corresponding vector and axial couplings. The values of $g^\alpha_{V,A}(f)$ depend on the particular choice of $U(1)'$. These couplings entirely encode any specific Z' model.

It is convenient to specify the $U(1)_\alpha$ charges of the left chiral components of both the fermion f and the conjugate antifermion f^c, denoted $Q_{\alpha f}$ and $Q_{\alpha f^c}$, respectively. The two sets of charges are related by

$$\epsilon^\alpha_L(f) = Q_{\alpha f}\,, \qquad \epsilon^\alpha_R(f) = -Q_{\alpha f^c}\,. \tag{3.5}$$

For example, the SM quarks u and u^c have, respectively, $U(1)_\alpha$ charges given by

$$Q_{1u} = \tfrac{1}{2} - \tfrac{2}{3}\sin^2\theta_W \qquad \text{and} \qquad Q_{1u^c} = +\tfrac{2}{3}\sin^2\theta_W\,.$$

The additional gauge couplings and charges, as well as the gauge boson masses and mixings, are model dependent.

3.2.1 Masses and Mass Mixings

The three and four point gauge interactions of a complex $SU(2)$ scalar multiplet ϕ can be read off from the kinetic term

$$\mathscr{L}^{\text{kin}}_\phi = (D^\mu\phi)^\dagger D_\mu\phi\,. \tag{3.6}$$

The diagonal (neutral current) part of the covariant derivate of an individual field ϕ_i is

$$D_\mu \phi_i = \left(\partial_\mu + ieq_i A_\mu + i\sum_{\alpha=1}^{n+1} g_\alpha Q_{\alpha i} Z^0_{\alpha\mu}\right)\phi_i \,. \tag{3.7}$$

where q_i and $Q_{\alpha i}$ are respectively the electric and $U(1)_\alpha$ charges of ϕ_i.

The neutral scalar fields ϕ_i acquire a vacuum expectation value in such a way that A_μ remains massless, while the $Z^0_{\alpha\mu}$ fields develop a mass term

$$\mathscr{L}_Z^{mass} = \tfrac{1}{2}\sum_{\alpha,\beta} M^2_{\alpha\beta} Z^0_{\alpha\mu} Z^{0\mu}_\beta \tag{3.8}$$

where

$$M^2_{\alpha\beta} = 2g_\alpha g_\beta \sum_i Q_{\alpha i} Q_{\beta i} \left|\langle\phi_i\rangle\right|^2 . \tag{3.9}$$

$M^2_{11} \equiv M^2_{Z^0}$ would be the (tree-level) Z mass in the SM limit in which the other Z^0's and their mixing can be ignored. If the only Higgs fields are $SU(2)$ doublets as in the SM, then

$$M^2_{Z^0} = \frac{1}{2} g_1^2 \sum_i \left|\langle\phi_i\rangle\right|^2 = \frac{1}{4} g_1^2 v^2 \tag{3.10}$$

where $v^2 = 2\sum_i \left|\langle\phi_i\rangle\right|^2 \sim (\sqrt{2}G_F)^{-1}$. A general Higgs structure allows Eq. 3.10 to become

$$M^2_{Z^0} = \frac{g_1^2}{4\sqrt{2}G_F\,\rho_0} \tag{3.11}$$

where

$$\rho_0 \equiv \frac{\sum_i (t_i^2 - t_{3i}^2 + t_i)\left|\langle\phi_i\rangle\right|^2}{\sum_i 2t_{3i}^2 \left|\langle\phi_i\rangle\right|^2} \xrightarrow{\text{singlet/doublet}} 1 \tag{3.12}$$

that is, ρ_0 remains equal to 1 provided that the scalar representation be a singlet or a doublet.

The physical massive bosons are obtained after diagonalizing the mass matrix (Eq. 3.9) . The $n+1$ massive eigenstates are

$$Z_{\alpha\mu} = \sum_{\beta=1}^{n+1} U_{\alpha\beta} Z^0_{\beta\mu} \tag{3.13}$$

where U is an orthogonal mixing matrix.

The case $n = 1$ corresponds to only one additional gauge boson. For this case

the mass matrix is

$$M^2 = \begin{pmatrix} 2g_1^2 \sum_i t_{3i}^2 \left|\langle\phi_i\rangle\right|^2 & 2g_1 g_2 \sum_i t_{3i} Q_{2i} \left|\langle\phi_i\rangle\right|^2 \\ 2g_1 g_2 \sum_i t_{3i} Q_{2i} \left|\langle\phi_i\rangle\right|^2 & 2g_2^2 \sum_i Q_{2i}^2 \left|\langle\phi_i\rangle\right|^2 \end{pmatrix} \equiv \begin{pmatrix} M_{Z^0}^2 & \Delta^2 \\ \Delta^2 & M_{Z'}^2 \end{pmatrix} . \tag{3.14}$$

The eigenvalues of 3.14 are the physical masses, given by

$$M_{1,2}^2 = \frac{1}{2}\left[M_{Z^0}^2 + M_{Z'}^2 \mp \sqrt{(M_{Z^0}^2 - M_{Z'}^2)^2 + 4\Delta^4}\right] \tag{3.15}$$

where U is the rotation

$$U = \begin{pmatrix} \cos\theta & \sin\theta \\ -\sin\theta & \cos\theta \end{pmatrix} \tag{3.16}$$

and

$$\theta = \frac{1}{2}\arctan\left(\frac{2\Delta^2}{M_{Z^0}^2 - M_{Z'}^2}\right) . \tag{3.17}$$

A possible implementation of a Extended $U(1)$ Model is the Sequential Standard Model (SSM) where the Z'_{SSM} boson is assumed to have the same couplings as for the standard Z boson. Using Eq. 3.4 and Eq. 2.20 lead to the vector and axial couplings for quarks

$$\begin{aligned} g_V^1(d) &= -1 + \tfrac{4}{3}\sin^2\theta_W = -0.693\,, & g_A^1(d) &= -1\,, \\ g_V^1(u) &= \quad 1 - \tfrac{8}{3}\sin^2\theta_W = \quad 0.387\,, & g_A^1(u) &= \quad 1\,. \end{aligned}$$

Similar expressions hold for the couplings with leptons

$$\begin{aligned} g_V^1(e) &= -1 + 4\sin^2\theta_W = -0.08 \quad , & g_A^1(d) &= -1\,, \\ g_V^1(\nu_e) &= \quad 1 \qquad\qquad\qquad\quad , & g_A^1(\nu_e) &= \quad 1 \end{aligned}$$

where we have taken $\sin^2\theta_W = 0.23$.

The superstring inspired E_6 theory is another example of an extended $U(1)$ model. The E_6 group has several intermediate breaking scales, for instance, it could break to a $SO(10)$ and a $U(1)_\psi$, *i.e.*,

$$E_6 \to SO(10) \times U(1)_\psi\,. \tag{3.18}$$

The $SO(10)$ itself is further broken to $SU(5)$ and a $U(1)_\chi$ gauge group, *i.e.*,

$$SO(10) \to SU(5) \times U(1)_\chi \,. \tag{3.19}$$

Finally, the $SU(5)$ is broken to the SM gauge group

$$SU(5) \to SU(3)_C \times SU(2)_L \times U(1)_Y \,. \tag{3.20}$$

The gauge fields corresponding to the groups $U(1)_\psi$ and $U(1)_\chi$ are not the mass eigenstates. As usual, the mass eigenstates Z' and Z'' are obtained via the rotation of the fields Z'_ψ and Z'_χ that diagonalises the mass matrix,

$$Z'(\theta) \equiv Z'_\psi \cos\theta + Z'_\chi \sin\theta \quad , \quad Z''(\theta) \equiv Z'_\psi \sin\theta - Z'_\chi \cos\theta \tag{3.21}$$

with θ being a parameter depending on the Higgs vacuum expectation value and the gauge couplings g_ψ and g_χ corresponding to $U(1)_\psi$ and $U(1)_\chi$.

The direct discovery channel of a neutral heavy resonances would be the observation of the resonance peak in difermion Drell-Yan channel. The dilepton channel provides very clean signals without much background. The most recent results of searches for exotic resonances decaying into a massive lepton pair $\ell^+\ell^-$ at a centre of mass energy of 8 TeV were reported by the CMS and Atlas collaborations. We present in Table 3.1 a summary of their results.

	CMS [25]	ATLAS [26]
sequential	2960	2860
ψ	2600	2380
χ	-	2540

Table 3.1: 95% CL lower limits on Z' gauge boson masses (GeV).

The CMS results exclude at 95 % CL, a sequential standard model $Z'_{\rm SSM}$ resonance lighter than 2960 GeV and a superstring-inspired Z'_ψ lighter than 2600 GeV, according to Fig. 3.2.

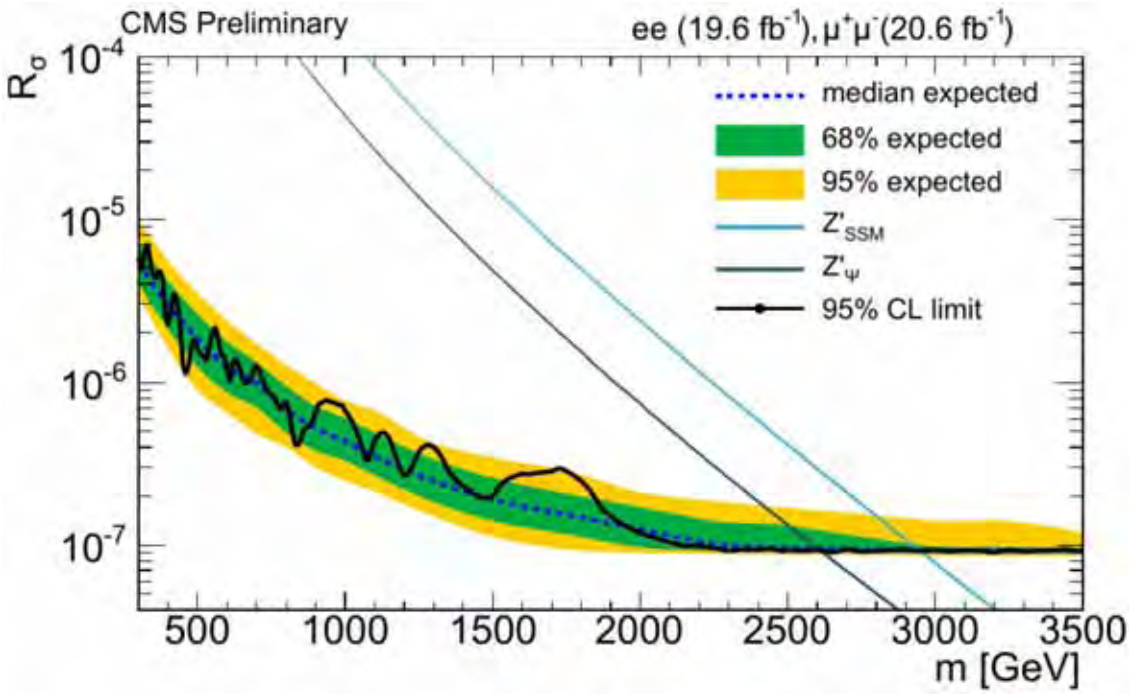

Figure 3.2: Upper limits on the production ratio R_σ of cross section times branching fraction into lepton pairs for Z'_{SSM} and Z'_ψ boson production to the same quantity for Z bosons [25].

3.2.2 Parameterization of the Z' Properties

Another way to observe neutral heavy resonances is through an intermediate decay into $W^\pm$ boson pairs. In fact, we dedicate the whole Chapter 5 to explore the possibilities of a diboson leptonic channel. From the phenomenological point of view [28–30], the study of process

$$pp \to Z' \to W^+W^- \to \ell^+\ell'^-\not{E}_{\text{T}} \tag{3.22}$$

requires the knowledge of the couplings of the new spin-1 states to the light quarks and to the electroweak vector boson pair, in addition to their masses and widths. Assuming that the coupling of the Z' to the gauge bosons have the same Lorentz structure as those of the SM, but with rescaled strength, the coupling $g_{Z'WW}$ must be bounded by

$$g_{Z'WW} \leq g_{Z'WW\,\text{max}} = g_{ZWW}\frac{M_Z}{\sqrt{3}M_{Z'}}\,. \tag{3.23}$$

This bound restores the unitarity in $W^+W^- \to W^+W^-$ [27] by the exchange of a Z'. The cross section for the process 3.22 can be written as

$$\sigma = \sigma_{\rm SM} + G\,\sigma_{\rm int}(M_{Z'}, \Gamma_{Z'}) + G^2\sigma_{Z'}(M_{Z'}, \Gamma_{Z'}) \tag{3.24}$$

with

$$G = \left(\frac{g_{Z'q\bar{q}}}{g_{Zq\bar{q}}}\right)\left(\frac{g_{Z'WW}}{g_{Z'WW\,\rm max}}\right) \tag{3.25}$$

where $g_{Z'q\bar{q}}$ is the Z' coupling to light quarks, and $g_{Zq\bar{q}} = g/\cos\theta_W$.

There are three free parameters in Eq. 3.24: the mass of the new spin-1 gauge boson $M_{Z'}$, its width $\Gamma_{Z'}$, and the combination of couplings G. The parameter $\Gamma_{Z'}$ is bounded by the inequality

$$\Gamma_{Z'} \geq \sum_{q=u,d} \Gamma(Z' \to q\bar{q}) + \Gamma(Z' \to W^+W^-)\,. \tag{3.26}$$

Rescaling the values of the partial widths (in GeV)

$$\Gamma(Z' \to u\bar{u}) = 0.3\left(\frac{M_{Z'}}{M_Z}\right)\left(\frac{g_{Z'q\bar{q}}}{g_{Zq\bar{q}}}\right)^2$$

$$\Gamma(Z' \to d\bar{d}) = 0.38\left(\frac{M_{Z'}}{M_Z}\right)\left(\frac{g_{Z'q\bar{q}}}{g_{Zq\bar{q}}}\right)^2$$

$$\Gamma(Z' \to W^+W^-) = 0.028\left(\frac{M_{Z'}}{M_Z}\right)^3\left(\frac{g_{Z'WW}}{g_{Z'WW\,\rm max}}\right)^2$$

it is possible to show that the minimum Z' decay width is

$$\Gamma_{Z'} \geq 0.27|G|\left(\frac{M_{Z'}}{M_Z}\right)^2 \text{ GeV}\,. \tag{3.27}$$

According to Eq. 3.27, for given values of G and $M_{Z'}$ there is a lower bound on $\Gamma_{Z'}$. However, that condition can be translated into a constraint on the parameter G for given values of $M_{Z'}$ and $\Gamma_{Z'}$.

Chapter 4

The LHC and the CMS Experiment

Today, the state-of-the-art experiments in the field of high energy physics are at the European Council for Nuclear Research (CERN), in Geneva, home of the Large Hadron Collider (LHC) and its complex of accelerators (Fig. 4.1).

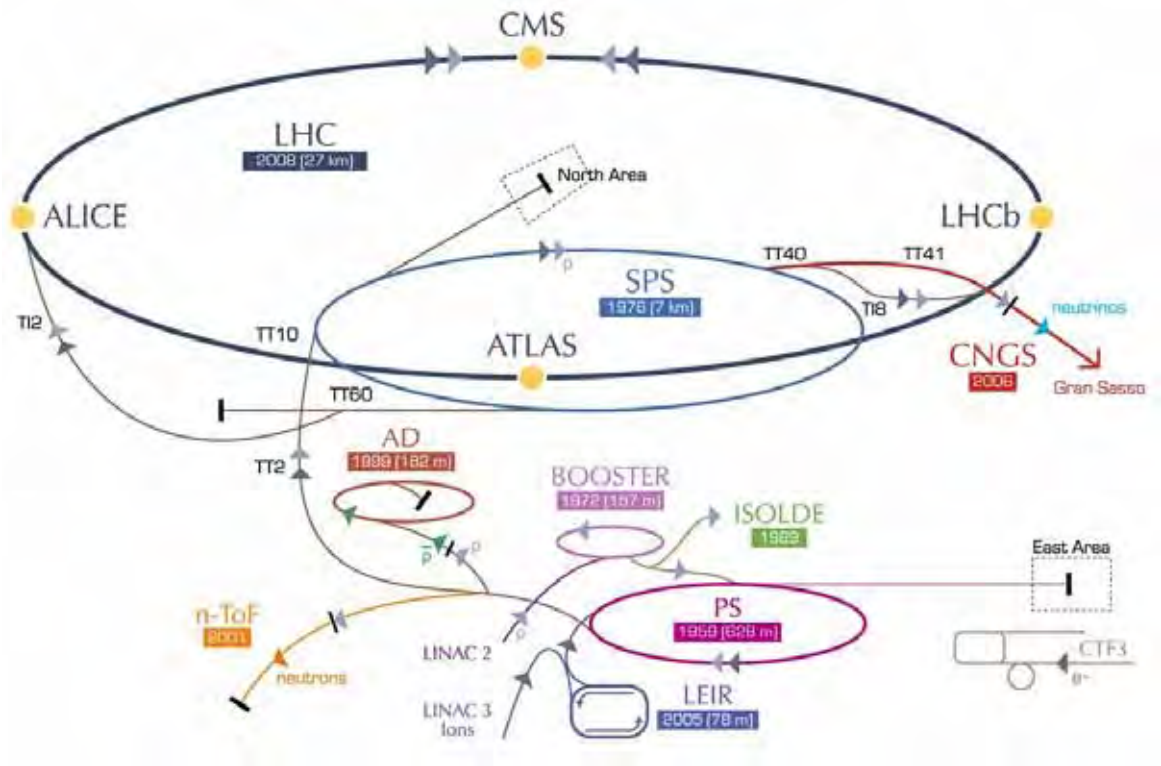

Figure 4.1: Overview of the CERN's Accelerator Complex [31].

The LHC is a circular accelerator with 27 km of circumference, installed in a tunnel 50 to 175 m underground. It was originally designed to collide protons at a centre of mass energy of 14 TeV with a design luminosity of 10^{34} cm^{-2}s^{-1}. In a circular accelerator, radio-frequency (RF) cavities provide the boost, while dipole superconducting magnets (Fig. 4.2) interspaced between the RF cavities supply the bending magnetic field that keeps protons in orbit.

The LHC circulates protons inside its beam-pipes not in a continuous stream

but in several very closely packed bunches, with each bunch made out of approximately 10^{11} particles. To maximise the probability of the protons colliding with one another, the LHC squeezes the beam within a transverse size of $\sigma_x \approx \sigma_y \approx 15\,\mu$m.

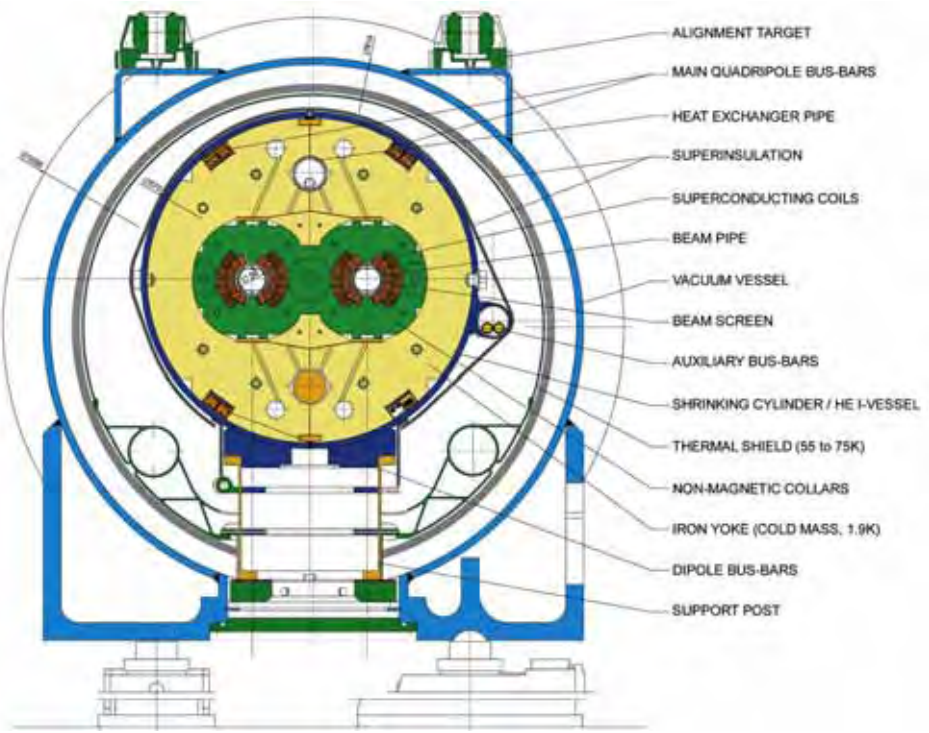

Figure 4.2: Dipole superconducting magnet [32].

Every 50 ns these bunches cross one another, and several proton-proton collisions take place. This is known as the pile-up; for the 2012 8 TeV operation parameters, there are in average of 20 interactions per bunch crossing. The event rate for a given process generated at the LHC collisions is given by $\mathcal{L} \times \sigma_i$, where σ_i is the cross section for the process under study and $\mathcal{L}$ is the instantaneous luminosity. The luminosity depends only on beam parameters such as the number of particles per bunch (n_1 , n_2 for the two beams), the revolution frequency (f) and the Gaussian widths of the beam profile in the horizontal and vertical plane (σ_x , σ_y)

$$\mathcal{L} = f \frac{n_1 n_2}{4\pi\sigma_x\sigma_y} \,. \tag{4.1}$$

The total number of events N_i produced at the collider in a time T involves the integrated luminosity $\mathcal{L}_{\text{int}}$,

$$N_i = \sigma_i \int_0^T \mathcal{L}\, dt \; = \sigma_i\, \mathcal{L}_{\text{int}} \,. \tag{4.2}$$

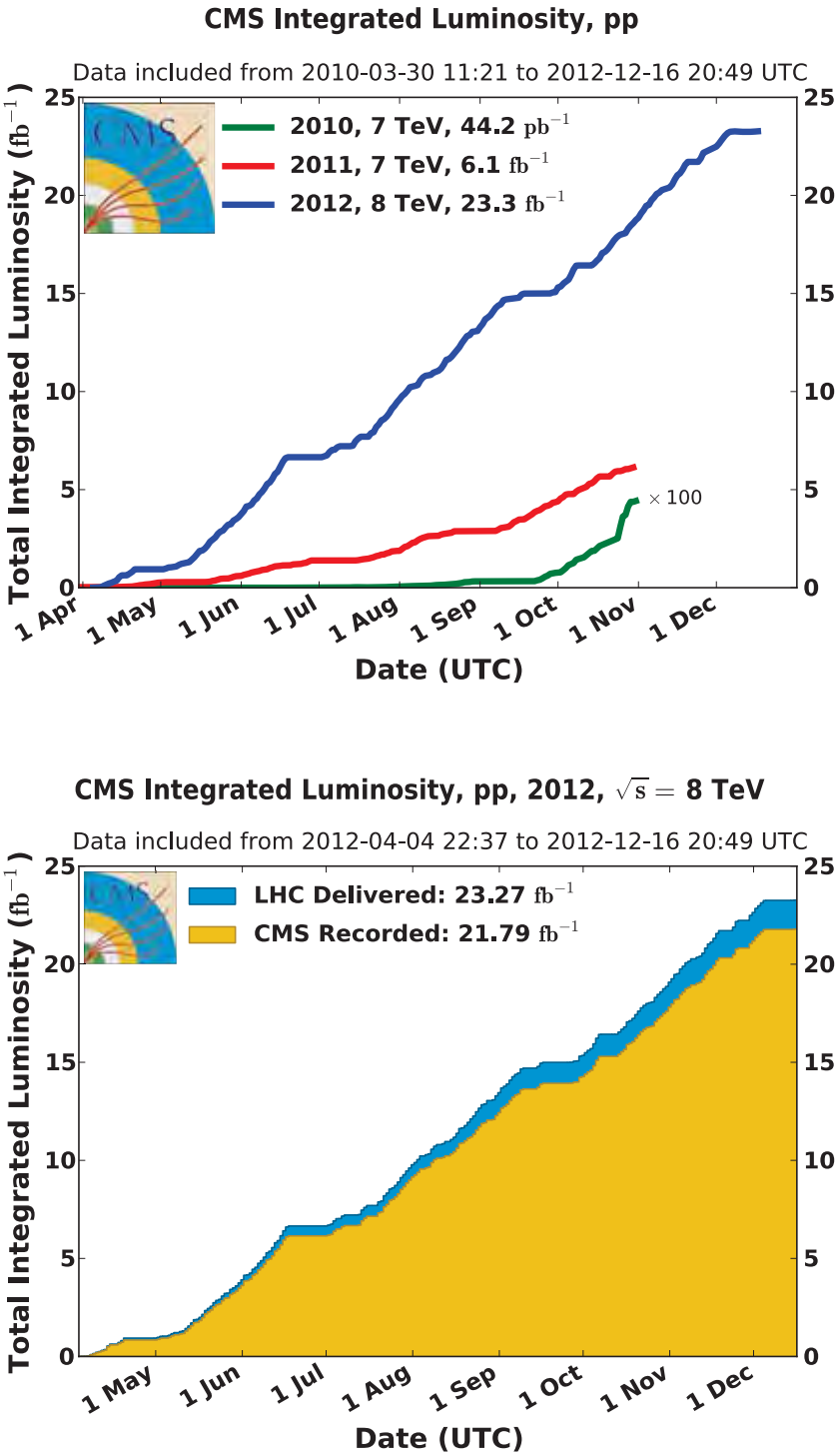

Figure 4.3: Performance of LHC over the period 2010-2012 (up). Luminosity delivered and recorded by CMS (bottom) for pp collisions at 8 TeV centre-of-mass energy in 2012 [33].

The first collisions at the LHC took place in 2010 using proton beams with a center of mass energy of 7 TeV. By the end of 2011, a data sample with integrated luminosity of 6 fb^{-1} was collected by CMS. In 2012 the center of mass energy was increased to 8 TeV and a further 23 fb^{-1} of data has been delivered, with a instantaneous peak luminosity approaching 8×10^{33} $cm^{-2}s^{-1}$.

The performance of LHC over the last three years of operation is summarized in Fig. 4.3. Throughout this period, LHC operated with 50 ns bunch spacing. The delivered luminosity is measured from the start of stable beams. The recorded luminosity is slightly lower than the delivered luminosity because the detector may fail and the recorded data are defective. The data taken when the detector is fully operational are encoded in the golden JSON file. Only the luminosity sections specified in the JSON file should be processed in physics analyses.

4.1 CMS Detector

The Compact Muon Solenoid (CMS) is one of the four main LHC experiments, and integrates the state-of-the-art detector technology with respect to particle identification. One special feature of CMS lies in the muon system. The muon is a minimum ionizable particle (MIP) what makes it harder to stop. Then, it is mandatory to build a large system to trace the muon's trajectory. The return magnetic field of the solenoid in the muon chambers gives the opportunity to bend the trajectory and measure the momentum, complementing the measurement made in the tracker. On the other hand, electrons lose energy by bremsstrahlung and come to stop rather quickly, so the Electromagnetic Calorimeter (ECAL) can be smaller. A smaller ECAL made of lead tungstate crystals is good to detect electrons, but cannot be used to stop muons.

The general layout of CMS can be seen in Fig. 4.4; its overall dimensions are 21.6 m length, 15 m diameter and 12,500 ton weight. CMS has a very compact design, high hermeticity and emphasizes good muon identification. It provides good charge and momentum resolution including efficient b and τ tagging capability as well as a good electromagnetic energy resolution and good missing transverse energy resolution.

The subdetectors are situated in an shell arrangement, and all the barrel systems have a forward equivalent to guarantee a 4π solid angle coverage. Studying the

layout in Fig. 4.4 more closely, one can observe additional very forward structures (muon detectors and a forward sampling calorimeter) to cover a high $|\eta|$ range.

CMS uses a right handed coordinate system in which the $+x$ axis points towards the center of the LHC ring, y points up, and $+z$ points along the direction of the beam. In a cylindrical system r is the radius from the nominal beam line and ϕ is the azimuthal angle. The pseudorapidity is defined as $\eta = -\ln[\tan(\theta/2)]$, where θ is the polar angle measured from the $+z$ axis. The transverse momentum is defined as $p_{\mathrm{T}} = p \cdot \sin\theta$, with p being the momentum.

4.1.1 Central System

The pixel detector is the innermost subsystem and the closest to the beam pipe, containing 66 million $100 \times 150\,\mu\mathrm{m}^2$ pixels responsible for track reconstruction and primary vertex identification as well as b-tagging. It is arranged in three barrel layers and two endcap disks at each end. The pixel detector is followed by a silicon strip system, which determines the momentum of electrically charged particles that traverse it. The system is structured in ten barrel layers and twelve endcap disks, composed of 9.3 million strips with pitch between 80 and 180 μm, with a total silicon surface area of 198 m^2.

4.1.2 Electromagnetic Calorimeter

The tracker is followed by an Electromagnetic Calorimeter (ECAL), which uses 75000 lead tungstate ($PbWO_4$) crystals to determine the energy of electrons and photons, producing light in proportion to the particle's energy. The ECAL is distributed in a barrel ($|\eta| < 1.479$) and two endcap ($1.479 < |\eta| < 3.0$) regions. Photodetectors placed in the back of each crystal detect the scintillation light and convert it to electrical signals. Electromagnetic showers are very narrow in lead tungstate (Molière radius of 21 mm), helping particle identification and the implementation of isolation criteria.

Preshower detectors consisting of two planes of lead followed by silicon sensors are located in front of the endcaps. When a photon passes through the lead layer it causes an electromagnetic shower containing electron-positron pairs, which are detected by the silicon sensors. From this the photon's energy is measured, whilst having two detector layers gives the particle's position. The preshower has a much

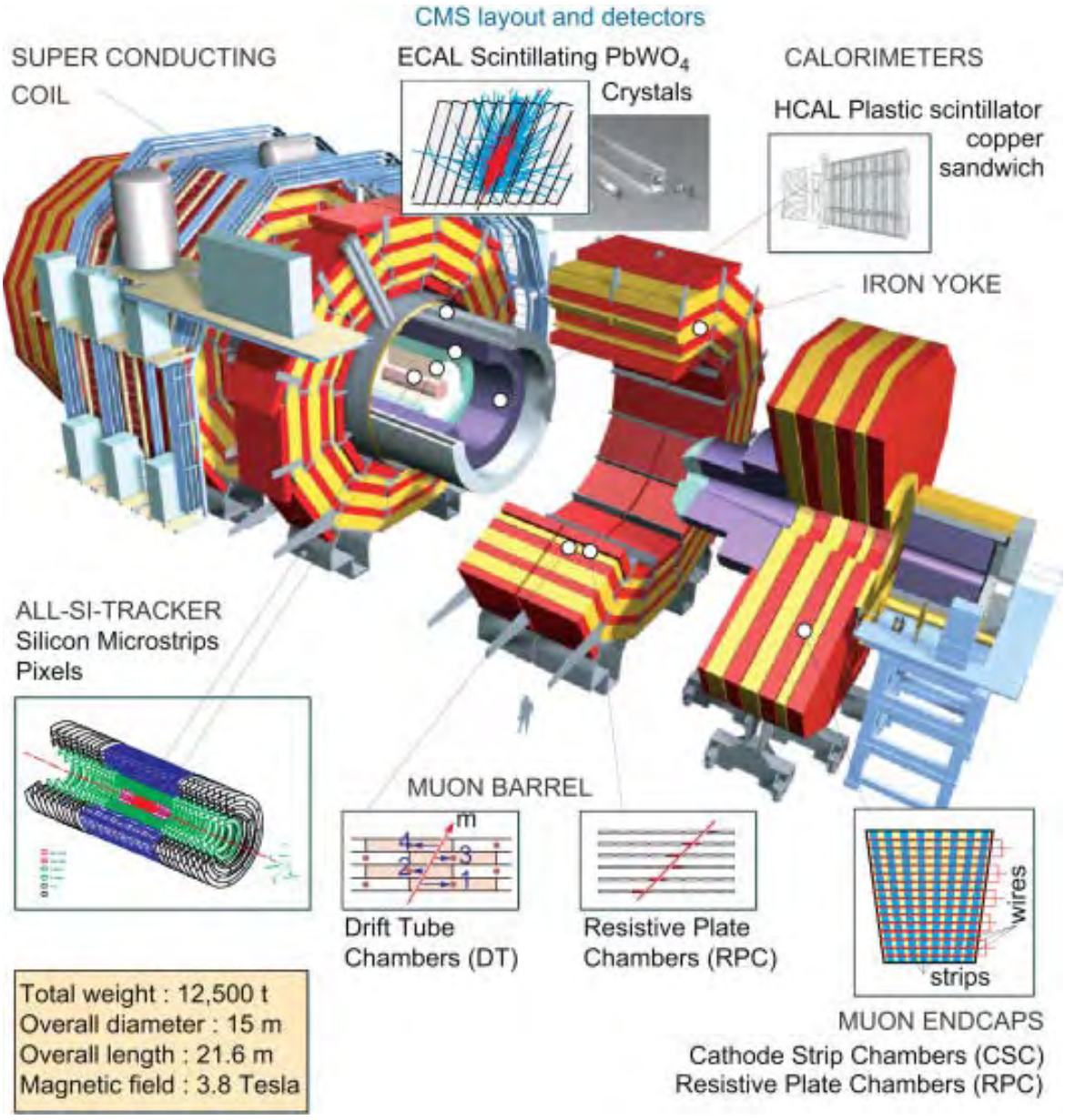

Figure 4.4: The CMS detector and its components [34].

finer granularity than the ECAL, with detector strips 2 mm wide compared to the 3 cm-wide ECAL crystals, what allows to distinguished closely-spaced photons.

4.1.3 Hadronic Calorimeter

The ECAL is surrounded by a brass/scintillator sampling Hadron Calorimeter (HCAL) to measure the energy of hadrons. Optical fibers collect up the light produced by the plastic scintillators and feed it into readout boxes where photodetectors amplify the signal. The HCAL covers the region $|\eta| < 3.0$. Their thickness varies from 7 to 10 interaction lengths depending on η; a scintillator placed outside of the coil at the innermost muon detector extends the instrument thickness to more than 10 interaction lengths everywhere. Quartz fibre and iron forward calorimeters, read out by photomultipliers, extend the calorimeter coverage in the range $3.0 < |\eta| < 5.0$.

4.1.4 Solenoid

The central feature of the CMS apparatus is a 13 m long and 6 m diameter superconducting solenoid, providing a magnetic field of 3.8 T. Within the field volume are the tracking devices and both calorimeters.

4.1.5 Muon System

Outside the solenoid is the muon system, the most visible part of CMS shown in Fig. 4.5. The CMS design relies on the high bending and excellent muon momentum resolution, which uses an iron return yoke interleaved with the muon chambers to increase the magnetic field. With the field parallel to the LHC beam axis, the muon tracks are bent in the transverse plane.

The iron yoke is instrumented with aluminum Drift Tubes (DTs) in the barrel ($|\eta < 1.2|$) and Cathode Strip Chambers (CSCs) in the end-cap region ($0.9 < |\eta| < 2.4$). Due to the iron yoke, the momentum resolution of the CMS muon system is dominated by the multiple scattering. The standalone muon momentum resolution is $\sigma(p_T)/p_T = 9\%$ for $p_T \leq 200$ GeV/c and 15 to 40% at $p_T = 1$ TeV/c, depending on η. Including the tracking system improves the result by an order of magnitude for low momenta. At 1 TeV the contribution of both measurements lead to a momentum resolution of about 5%.

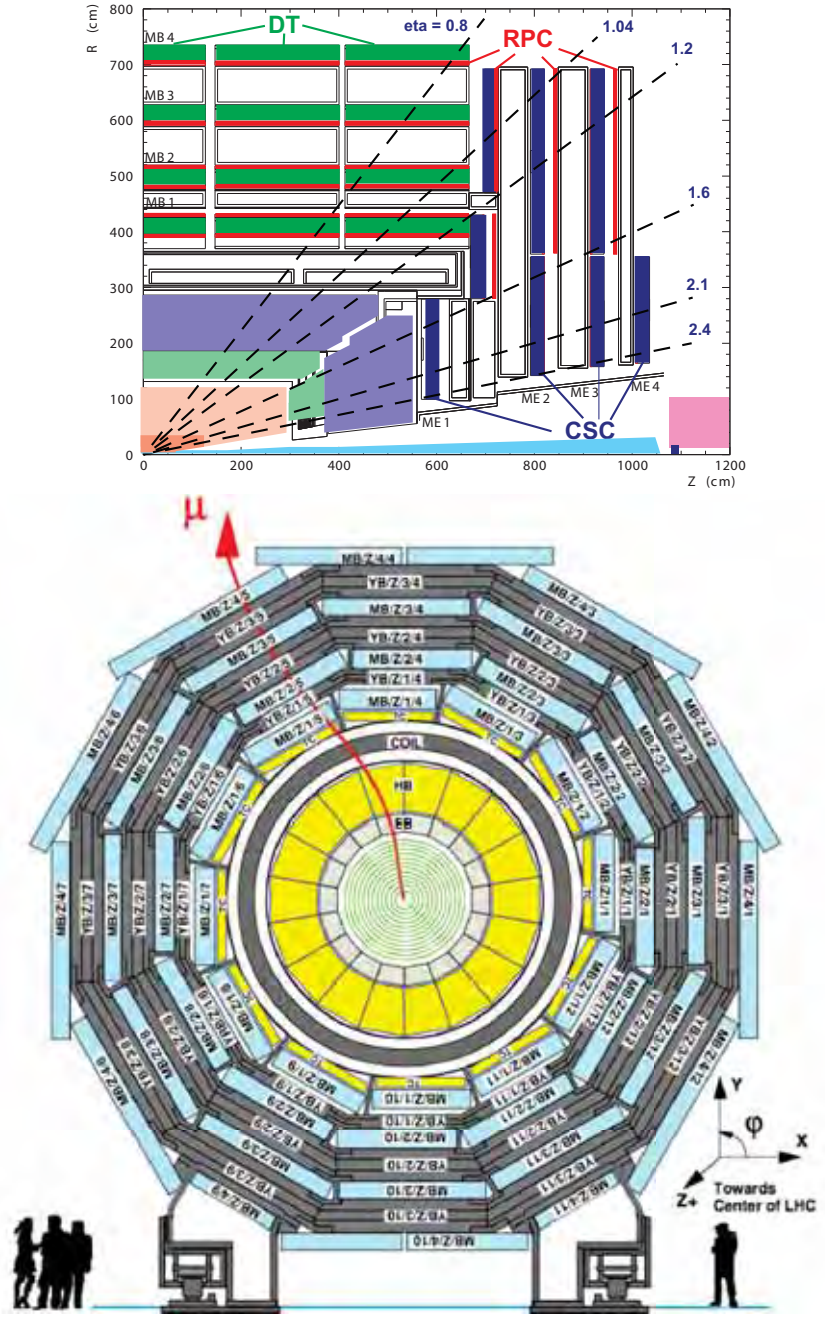

Figure 4.5: Pseudorapidity coverage of the muon system, and muon track in the transverse plane [35].

The DT and CSC subsystems can each trigger on muons with large transverse momentum in the range $|\eta| < 2.4$. However, for the full LHC luminosity, faster trigger chambers are needed to associate the detected muons to the right crossing of proton bunches. Resistive Plate Chambers (RPCs) covering the region $|\eta| < 1.6$ are used by the muon system for fast trigger.

4.2 Particle Identification

The identification of stable particles in CMS relies on the different interactions of a particle with the subdetectors. While photons, electrons and hadrons lose most of their energy and stop in the calorimeters, muons deposit only a small fraction of their energy through ionization so they reach the outer part of the detector, where the muon chambers are located. These characteristic signatures (Fig. 4.6) based on tracking and calorimetry are crucial aspects for Particle Identification [38].

The subdetectors in CMS are stacked in radial layers and a particle passes through these layers sequentially from the collision point outward: first the tracking system, then the electromagnetic and hadronic calorimeters, finally the muon system. All layers are embedded in a magnetic field in order to bend the tracks of charged particles for momentum and charge sign determination.

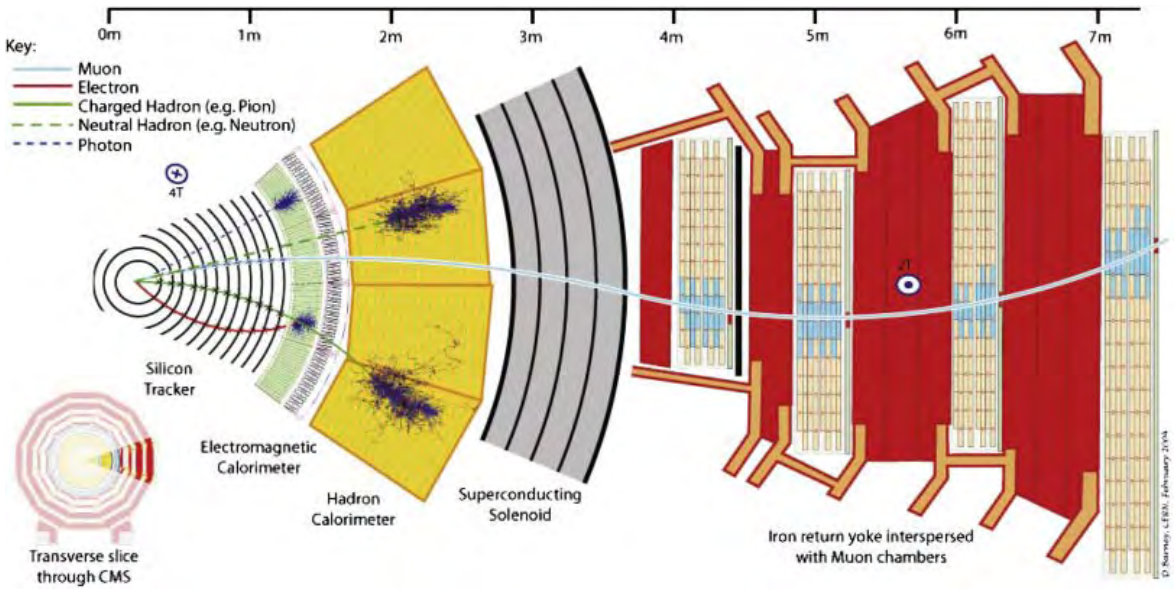

Figure 4.6: Characteristic signatures of different particles in CMS [34].

4.2.1 Missing Energy

Neutrinos produced in the final state escape from the detector causing an energy imbalance in the observed event. Momentum conservation is the available way to reveal the presence of neutrinos. Since the z-component of the momentum of the colliding partons is not known, one cannot determine the net missing energy caused by neutrinos.

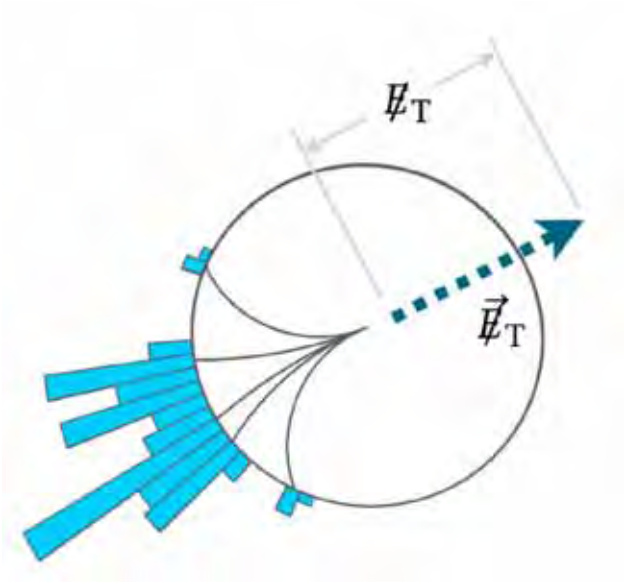

Figure 4.7: Missing transverse momentum and its magnitude.

However, the total momentum in the transverse plane is zero to a very good approximation. One can define the missing transverse momentum as the negative vector sum of the transverse energies of all final-state particles reconstructed in the detector. The missing transverse energy $\not{E}_T$ corresponds to the magnitude of the missing transverse momentum (Fig. 4.7).

$$\vec{\not{E}}_T = -\sum_i \vec{E}_T^{\,i} \tag{4.3}$$

CMS has implemented four major types of algorithms to reconstruct $\not{E}_T$ [36]: (i) caloMET based on calorimeter energies using the tower geometry of the hadron calorimeter, (ii) track-corrected MET calculated by replacing the calorimeter tower energies matched to charged hadrons with their corresponding charged-track momenta, (iii) pfMET calculated through a complete particle-flow technique, (iv) $\not{H}_T$ calculated through reconstructed jets.

In our study we used the pfMET algorithm [37], which takes advantage of the versatility of the CMS apparatus to identify and reconstruct individually each particle combining the information from all sub-detectors.

4.2.2 Track Reconstruction

The track reconstruction uses an iterative procedure [39] consisting of a number of steps to select better tracks first and removing their hits, before other tracks are reconstructed from the remaining hits. Each of the tracking steps starts with a collection of seeds formed from 2 (a pair seed) or 3 (a triplet seed) pixel hits consistent with some minimum track p_{T}, and coming from some region of the beam spot. The first steps use triplet seeds and higher minimum track p_{T}, these are followed by steps using pair seeds and lower p_{T}. The later steps use seeds that contain hits from the silicon strip detector to find detached tracks, *e.g.* from decay products of K_s^0 mesons or Λ^0 baryons.

4.2.3 Primary Vertex Reconstruction

CMS has to observe the decay products of various particles produced and work backwards to determine which collision interactions produced which particles. In the CMS tracker (made up of silicon pixels and strips), the number of hits grows linearly with pile-up. As these hits need to be combined into tracks, the number of possible combinations that make a track grows fast with pile-up. Fortunately, the high granularity and efficiency of the tracker provides the means to distinguish the many tracks in an event (Fig. 4.8).

The vertex reconstruction can be seen as a clustering procedure in which each vertex is a cluster of tracks selected by a fitting algorithm. Reconstructed primary vertices are required to have a z position within 24 cm of the nominal detector center and a radial position within 2 cm of the beamspot. There must also be more than four degrees of freedom in the fitted vertex.

4.2.4 Jets Reconstruction

Jets are the experimental signatures of quarks and gluons produced in high-energy processes such as head-on proton-proton collisions. As quarks and gluons have a net color charge and cannot exist freely due to color-confinement, they are

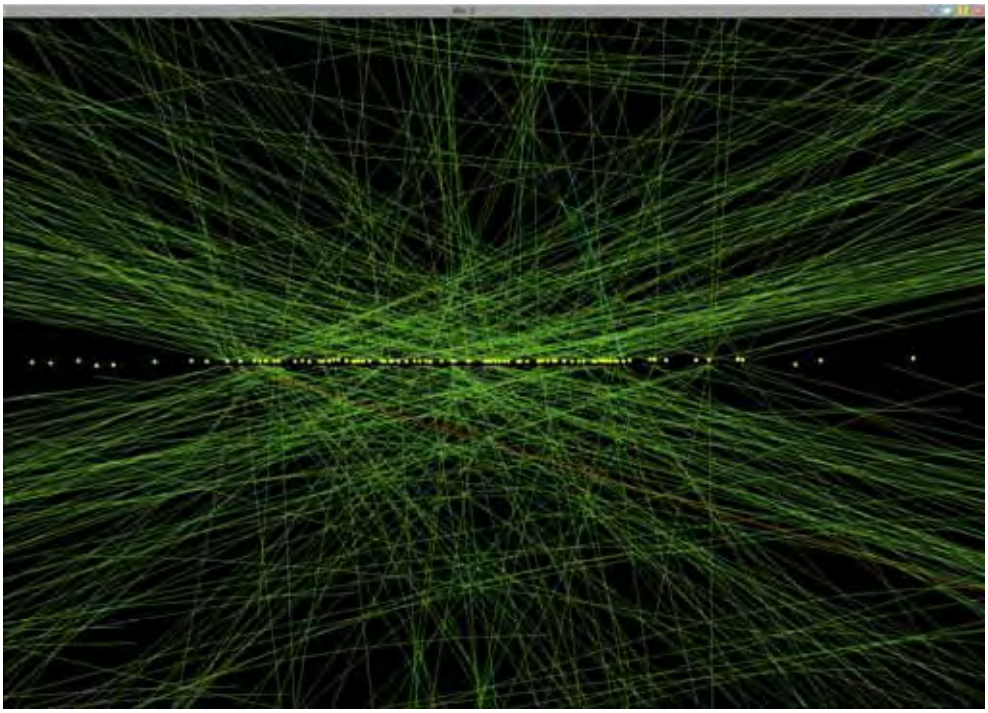

Figure 4.8: Tracks and pileup in a typical collision. [34]

not directly observed in Nature. Instead, they come together to form colorless hadrons, a process called hadronization that leads to a collimated spray of hadrons called a jet (Fig.4.9).

As these jets of particles propagate through the CMS detector, they leave signals in components such as the tracker and the electromagnetic and hadronic calorimeters. These signals are combined using jet algorithms to form a reconstructed jet. However, the energy of the reconstructed jets does not correspond to the true particle-level energy, which is independent of detector response; jet energy corrections relate these two values. The detailed understanding of the jet energy scale is of crucial importance for many physics analyses, and it is often an important component of their systematic uncertainty.

Within CMS, three different methods to reconstruct jets are supported with jet energy corrections: *i*) a calorimeter-based approach; *ii*) the Jet-Plus-Track approach, which improves the measurement of calorimeter jets by exploiting the associated tracks; *iii*) the Particle Flow approach, which attempts to reconstruct individually each particle in the event, prior to the jet clustering, based on information from all relevant sub-detectors. The significantly improved resulting jet energy resolutions, especially at low transverse momentum, indicate that the

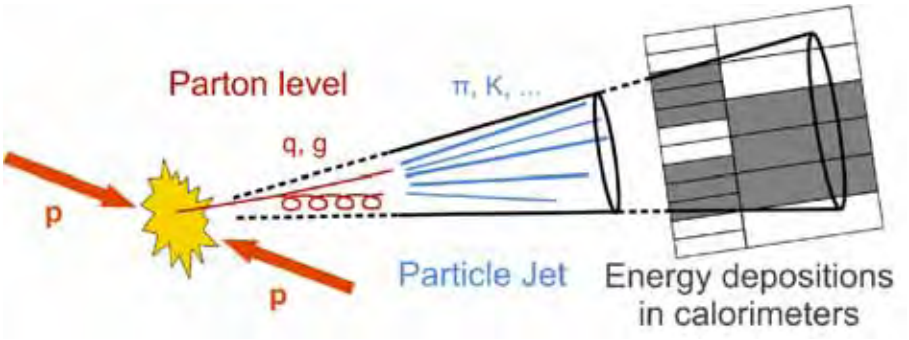

Figure 4.9: pp collision and the resulting collimated spray of particles, a jet.

Particle Flow approach offers advantages with respect to the other types. Indeed, it is used by most physics analyses within CMS.

Matching by ΔR

Matching means the association of objects from different collections based on their similarity in spatial coordinates and/or kinematics. It is useful to validate the proper reconstruction of physical objects such as muons, electrons or jets. For example, given a reconstructed jet (recJet) we associate a generated jet (genJet) based on the ΔR distance defined as

$$\Delta R = \sqrt{(\Delta\phi)^2 + (\Delta\eta)^2} \tag{4.4}$$

where $\Delta\phi$ is the azimuthal separation between the objects and $\Delta\eta$ measures their polar separation. Around each reconstructed jet we search for generated jets within a cone of aperture ΔR, as shown in figure 4.10.

Those jets that do not match any generated jet might be either mis-reconstructed or due to pile-up, so it has to be rejected from the collection of physical objects. Recall that matching is useful for any physical object, but it is viable only in Monte Carlo studies when the list of generated objects is known beforehand.

4.3 Software and Computing

The Monte Carlo (MC) method is a numerical technique for calculating probabilities and related quantities by using sequences of random numbers [40]. Of great interest in physics are the MC event generators, they include matrix element calculators like Alpgen [42] and MadGraph [43], and multi-purpose MC generator

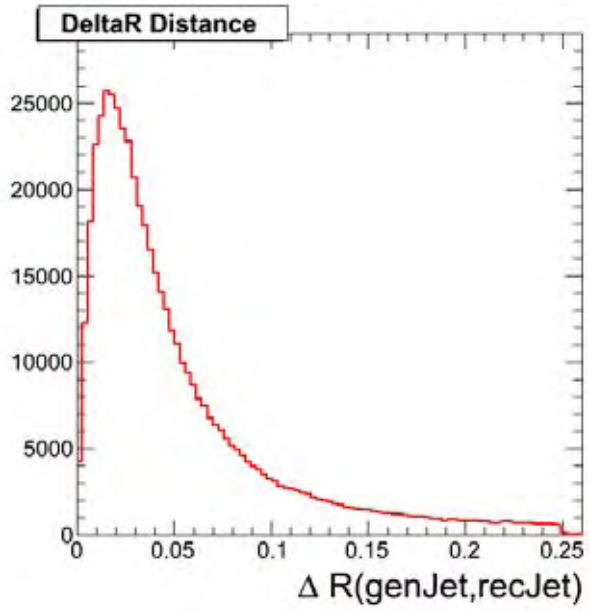

Figure 4.10: ΔR separation between generated and reconstructed jets.

like PYTHIA [41]. Matrix element calculators deliver an event at the parton level, then MC generators can further be used to develop a fully hadronized event.

PYTHIA provides the generator level of what happens in a particle collision: implements models for a number of physics aspects, such as hard and soft interactions, parton distributions, initial and final state radiation, multiple interactions, fragmentation and decay, and hadronization of the parton-level events. However, the generation of events is only the first step in the complete analysis chain.

4.3.1 Simulation and Recontruction

The detailed simulation and reconstruction of physics events is extremely time consuming. The analysis chain is decomposed into four major steps as follows:

1. Generation of Monte Carlo events. The Monte Carlo events are created using generators like PYTHIA. These generators produce a list of particles and their four-vectors.

2. Simulation of material effects. This is the most time consuming step. The output of this step is called *SimHits*. They contain the information about the energy stored in different detector elements at different times.

3. Simulation of readout electronics (digitalization). The detector converts the

energy deposited by the particles into electronic signals that are converted to digital information. Since the simulation of material effects requires large amount of CPU time, the minimum bias events are randomly selected from a large pool of simulated events and combined with the simulated signal events. The combination of minimum bias events with a signal event and the simulation of the detector response to the energy deposition are performed by the reconstruction software. The output created in this step is called *DIGIs*.

4. Reconstruction of physics/analysis objects. The reconstruction is performed in several sub-steps. First the *DIGIs* are combined to reconstructed hits *RecHits*, which for example combine several strips of the silicon tracking detectors. Then *RecHits* are used to find tracks in the inner tracker and the muon chambers and clusters in the calorimeters. The reconstruction can produce more complicated objects like jets or information about the missing energy and finally physical objects like electrons, photons, muons etc.

4.3.2 Data Analysis with CMSSW

The results presented in this dissertation are based on Monte Carlo samples generated and analyzed with the CMSSW framework [56], the CMS Software tool for data processing. The huge amount of data collected by CMS requires large resources for storage and containers to organize them in different *events*. The concept *event* is related to a computational class within the CMSSW.

The CMS software (CMSSW) consists of over a thousand subpackages providing an extensive toolkit for users to carry out analysis of data. It also gathers services needed by the reconstruction modules that process the data. The CMSSW executable, called cmsRun, is configured at run time by the user's configuration file. This file tells cmsRun which data to use, which modules to execute, which parameter settings to use for each module, and how the events are filtered.

More important than the software itself is the data which contains the information we finally want to extract. The data is organized in *events*, and according to the event data model (EDM) each event is a C++ object container for the reconstructed data related to a particular collision (Fig. 4.11): physical particles are accessed through C++ objects.

An *event* starts as a collection of the RAW data from the detector or Monte Carlo. As the event data is processed, products are stored in the *event* as reconstructed

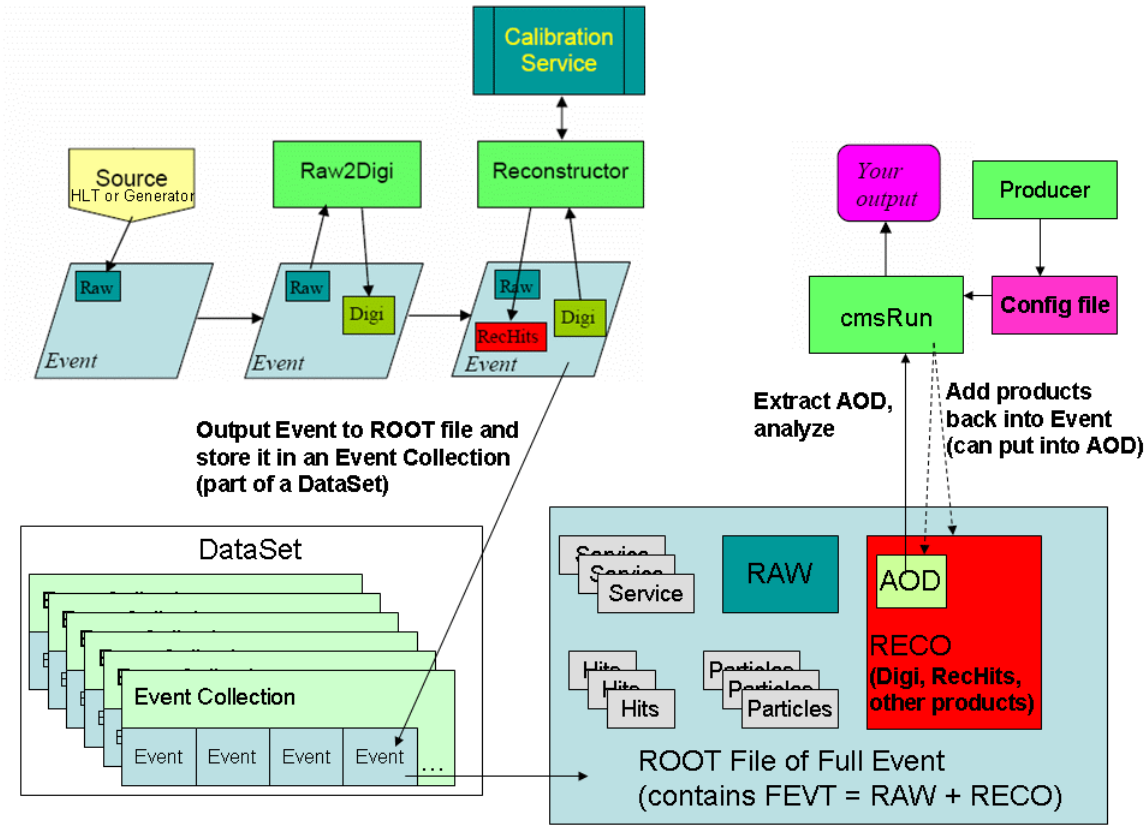

Figure 4.11: The Event Data Model

(RECO) data objects. The *event* also contains metadata describing the configuration of the software used for the reconstruction of each contained data object and the conditions and calibration data used for such reconstruction. The event data is output to files browsable by ROOT [44].

The full event data (FEVT) in an *event* is the RAW plus the RECO data. Analysis Object Data (AOD) is a subset of the RECO data in an *event*; AOD alone is sufficient for most kinds of physics analysis. Figure 4.11 illustrates how an *event* changes as data processing occurs.

4.3.3 Computing Infrastructure

CMS makes use of a grid of computers connected together in an hierarchical organization so that users around the world can share data and computational power. The structure called Worldwide LHC Computing Grid (WLCG) is divided in clusters of computers called Tiers which are classified depending on their

computational power and storage capacity.

- Tier 0: The Tier T0 is located at CERN, where all raw information coming from the detector is saved, reconstructed, and later on transmitted to the rest of the chain.
- Tier 1: There are several national T1 sites around the world, providing storage and redistribution for MC events generated by the T2's.
- Tier 2: There T2 centers provides capacity for user analysis, calibration studies, and Monte Carlo production for the whole experiment.
- Tier 3: Any small cluster of computers installed at an institute providing local access to the Grid.

The São Paulo Research and Analysis Center (SPRACE) was implemented in 2003 to collaborate with the DØ and CMS experiments. SPRACE hosts a T2 in the CMS computing structure providing around 10 Teraflops of computing power and 800 TB of storage space. During the development of this work we have extensively used the resources of the T2-BR-SPRACE center to analyze data, bring/send datasets from/to other tiers, and run Monte Carlo simulations.

Chapter 5

Diboson Leptonic Channel

5.1 Electroweak Measurements

The study of electroweak processes in pp collisions provides an important test on the SM. Any deviation of the measured cross sections from SM predictions, after being thoroughly verified for factors like theoretical mismodelings, detector effects and statistical fluctuations, would indicate the presence of new physics. The agreement between SM predictions and measured cross sections (see Fig. 5.1) gives confidence in the reliability of the theoretical calculations and in the detector performance.

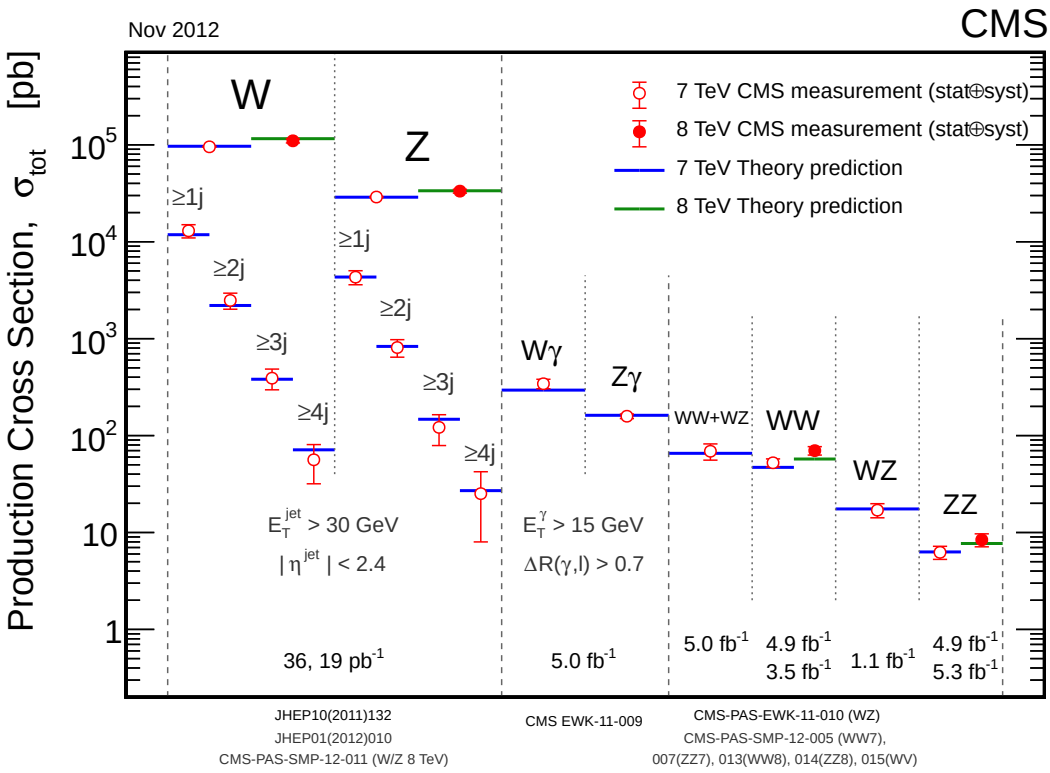

Figure 5.1: Vector boson production cross-sections measured by CMS [45].

The diboson WW production is one of the SM precision measurements performed at CMS [46]. A resonances in the WW transverse mass spectrum can be the signature of new phenomena and can be interpreted accordingly to many BSM models involving neutral heavy spin-1 resonances or massive spin-2 gravitons [47].

It is worth to remind the decay modes of a W^+ boson which are presented in Table 5.1. The decay mode into hadrons has a larger fraction than the mode into leptons, but the high detection efficiency and low reconstruction fake rate of muons and electrons may turn leptonic channels more attractive than the hadronic one. Moreover, due to the presence of leptons in the final state, the magnitude of the QCD background is diminished; this is due to the fact that leptons are not subject to the strong interaction.

Mode	Fraction
$e^+\nu$	10.75 %
$\mu^+\nu$	10.57 %
$\tau^+\nu$	11.25 %
$\ell^+\nu$	10.80 %
hadrons	67.60 %

Table 5.1: Decay modes of a boson W^+. ℓ is the average of the leptonic modes [48].

A diboson WW can decay into a fully leptonic, semileptonic, or fully hadronic channel, as indicated in Table 5.2.

Mode	Fraction
$\ell^+\nu_\ell\,\ell'^-\nu_{\ell'}$	1.2 %
$\ell^+\nu_\ell\,q\bar{q}$	7.3 %
$q\bar{q}\,q\bar{q}$	46 %

Table 5.2: Decay modes of a diboson W^+W^-.

In this work we have chosen to study only the fully leptonic channel, in order to both avoid the more complicated techniques needed to work with jets and to take advantage of the great performance of CMS at muon and electron reconstruction.

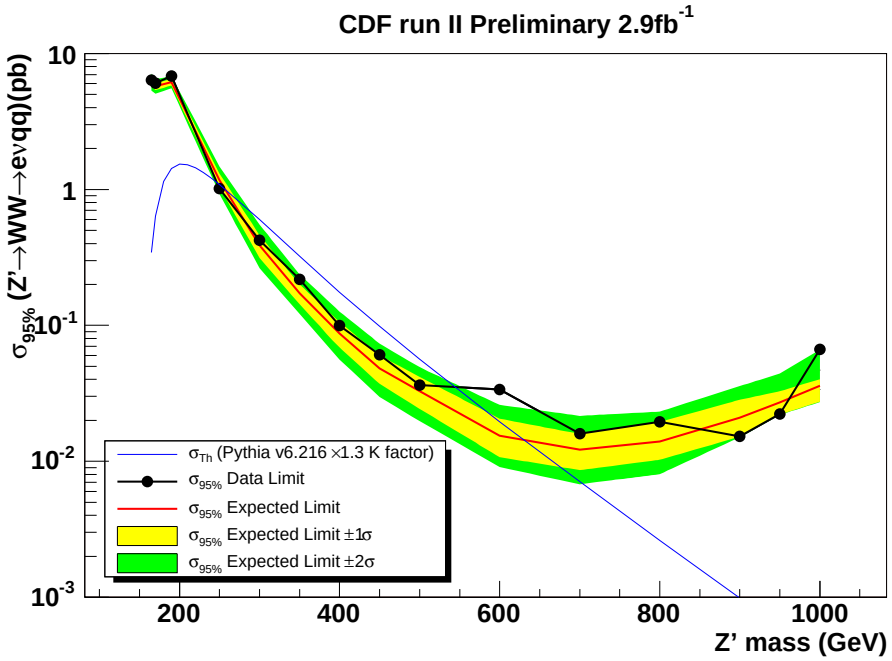

(a) Cross section × branching ratio limits at 95% CL for Z' (CDF Collaboration [49]).

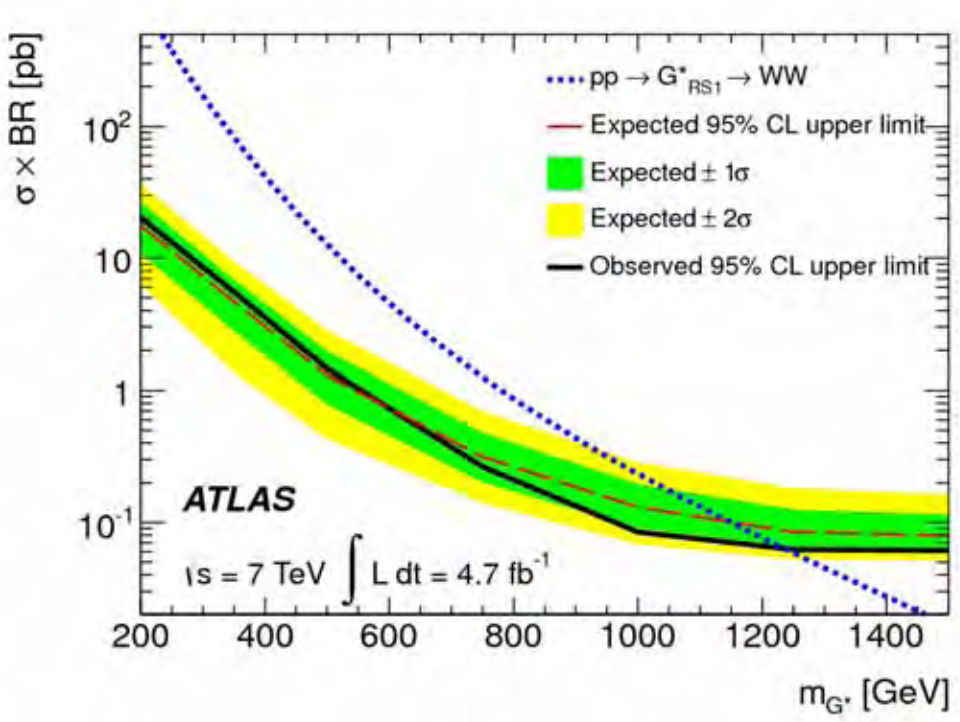

(b) The observed and expected 95% CL upper limits on $\sigma \times BR$ for the RS graviton (Atlas Collaboration [52]).

Figure 5.2: Searches for WW resonances in hadron colliders.

Searches for WW Resonances

Searches for WW resonances in the fully leptonic and semileptonic channels were reported by Tevatron experiments. Direct searches for heavy WW resonances were performed by the CDF collaboration [49], setting limits on the cross section $\sigma(p\bar{p} \rightarrow WW)$ in proton-antiproton collisions at $\sqrt{s} = 1.96$ TeV. The Z' mass exclusion region obtained from Fig. 5.2(a) corresponds to 257–630 GeV. Studying the same WW channel, the DØ collaboration reported limits on a spin-2 Randall-Sundrum (RS) [13] graviton in the range 300–754GeV at 95% CL [50].

Recently, LHC experiments also performed searches for exotic resonances. The CMS collaboration set 95% CL upper limits on the cross section for resonances decaying to qW, qZ, WW, WZ, or ZZ final states [51]. The ATLAS collaboration set limits using a RS graviton model and its extension, the bulk RS graviton model [47], as benchmarks. The lower limit on the RS gravitons was set to 1.23 TeV according to Fig. 5.2(b).

5.2 $pp \rightarrow Z' \rightarrow W^+W^-$: Signal Simulation

We explored the feasibility of observing exotic Z' resonances decaying into WW pairs according to the reaction depicted in Fig. 5.3. It represents a proton-proton collision producing a Z' that couples to light quarks. The exotic resonance then decays into a pair of W bosons, that consequently decay into leptons of opposite electric charge. A pair of neutrinos emerge from the W decay so we expect missing transverse energy present in the event.

We used CMS Fast Simulation (FastSim) [53], a CMSSW-integrated tool [56] to simulate and reconstruct events with the CMS detector. FastSim gives an accurate simulation of the detector effects without the CPU time consuming of the full simulation based on GEANT [54]. GEANT simulates particle transport in matter considering processes like bremsstrahlung, pair production, Compton scattering, and nuclear interactions. Those interactions generate cascades of new particles, originating particle showers. Then GEANT also simulates the interaction with the sensitive elements of the detector, and gives as final answer the charge deposited or the light yield in each element. It's a time-consuming process. FastSim, on the other hand, uses parametrized showers and responses for the sensors, saving between one and two orders of magnitude in time.

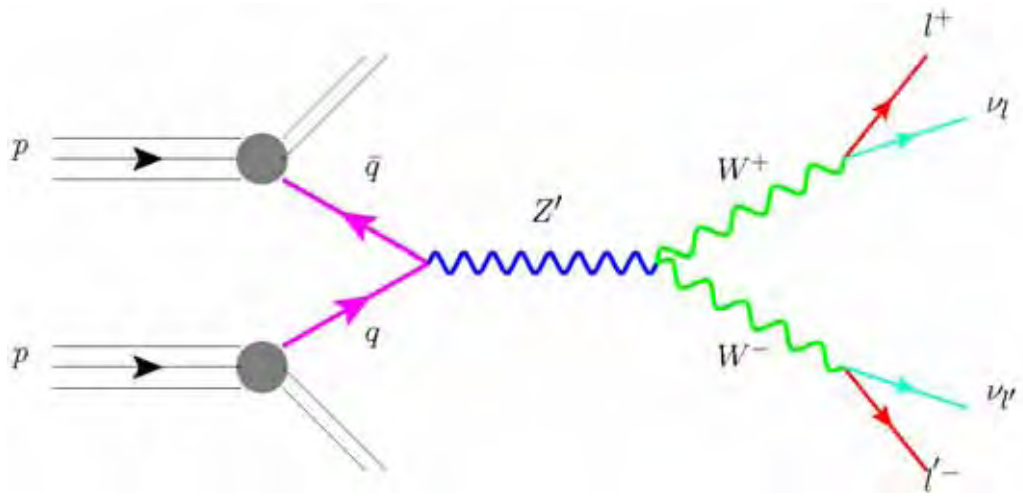

Figure 5.3: $pp \to Z' \to W^+W^-$ leptonic channel.

The Physics Analysis Tool (PAT) [55] is a high–level analysis layer which provides access to the algorithms in the framework of the CMSSW offline software. Although this work only analyses Monte Carlo events, the PAT has the capabilities to access and treat events from collision data, which may be useful in a forthcoming step of this work.

The Z' events were generated with PYTHIA 8.153* which provides values for the cross section,

$$\sigma(pp \to Z' \to W^+W^-)$$

at the center-of-mass energy $\sqrt{s} = 8$ TeV, multiplied by the branching ratio for leptons,

$$BR(W^+W^- \to \ell^+\nu_\ell\, \ell'^-\nu_{\ell'})$$

where ℓ indicates a muon or electron, and ν_ℓ the respective neutrino. The result is presented in the Fig. 5.4. We have taken four different values for the mass $M_{Z'} = 0.5$, 1, 1.5, and 2 TeV.

5.2.1 Z' Couplings to Quarks and Vector Bosons

We assumed that the couplings between the Z' and light quarks are the same as the ones of the standard Z boson. Furthermore, they were assumed generation–independent, requiring only eight numbers to parameterize the vector and axial

*There are specialized generators [JHU Generator, http://www.pha.jhu.edu/spin/] that include full spin and polarization correlations. PYTHIA does not take into account these correlations.

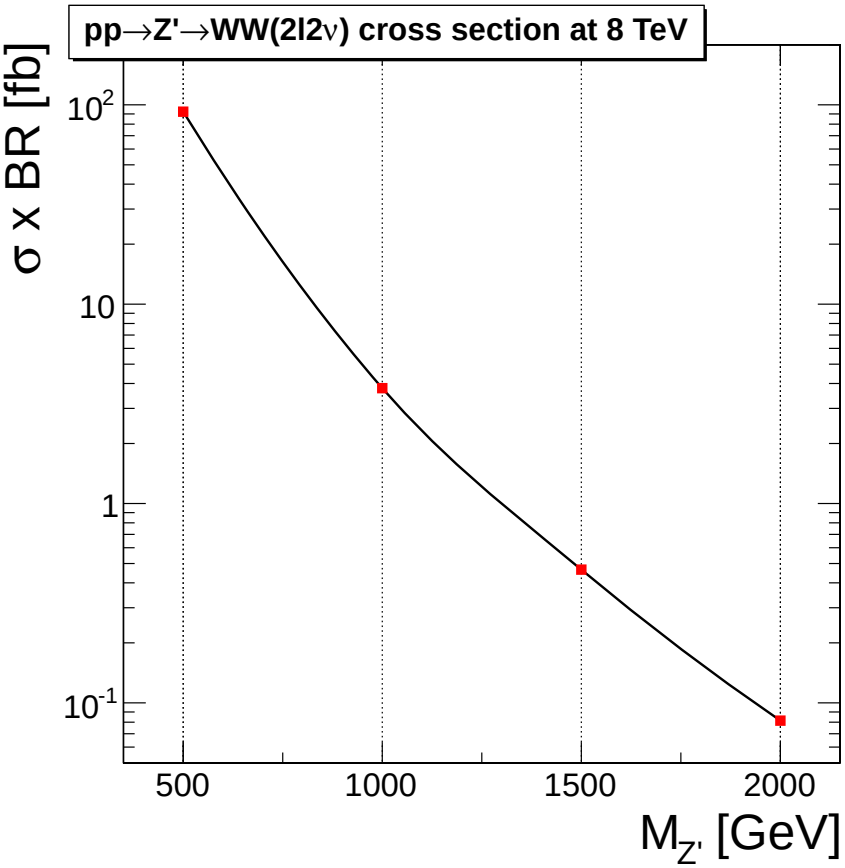

Figure 5.4: $pp \to Z' \to W^+W$ cross section in the leptonic channel.

couplings. The parameters available in PYTHIA to implement these couplings are listed in Table 5.3.

	Vector coupling	Axial coupling
d quarks	`Zprime:vd` (-0.693)	`Zprime:ad` (-1)
u quarks	`Zprime:vu` (0.387)	`Zprime:au` (1)
e leptons	`Zprime:ve` (-0.08)	`Zprime:ae` (-1)
ν_e neutrinos	`Zprime:vnue` (1)	`Zprime:anue` (1)

Table 5.3: PYTHIA parameters for the Z' couplings to quarks and leptons and their default values.

The coupling of Z' with the vector boson pair W^+W^- was assumed to be,

$$g_{Z'WW} = g_{ZWW} \left(\frac{M_W}{M'_Z} \right)^2 \tag{5.1}$$

as in the extended gauge model of reference [59]. By default this coupling is off, but can be switched on through the PYTHIA parameter `Zprime : coup2WW`. With this parameter, PYTHIA calculates the coupling $g_{Z'WW}$ according to the expression

$$g_{Z'WW} = (\texttt{Zprime : coup2WW}) \times \left(\frac{M_W}{M_{Z'}}\right)^2 \times g_{ZWW}\,. \tag{5.2}$$

Two different cases, corresponding to the reference model and the extended gauge model, are shown in Fig. 5.5.[†]

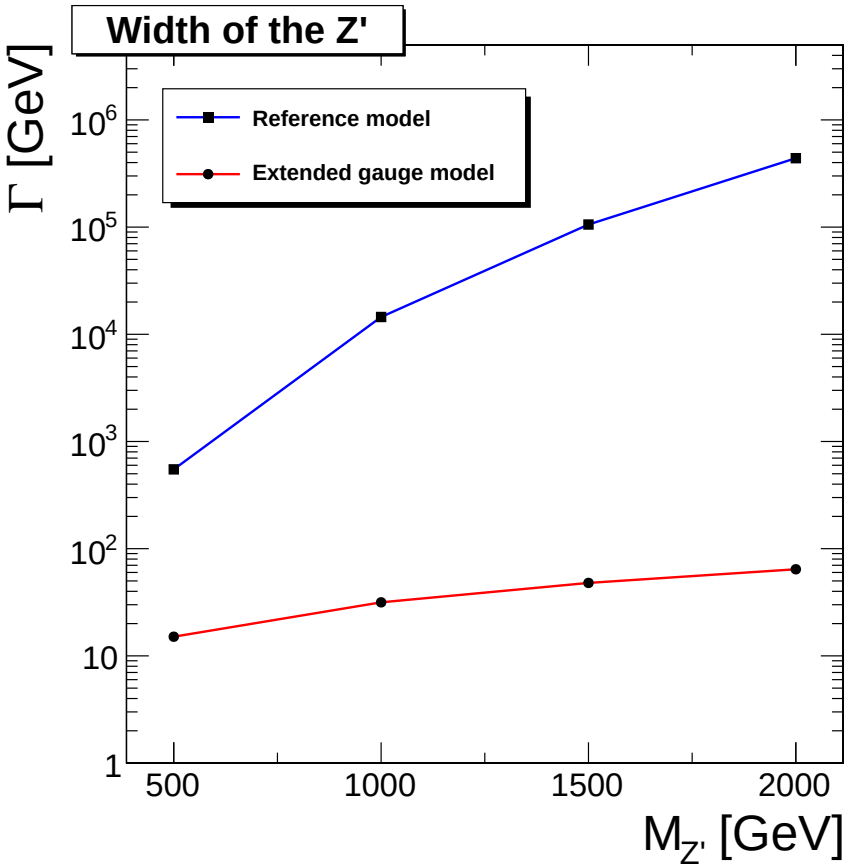

Figure 5.5: Width of the Z' into the channel WW for two models assuming different $g_{Z'WW}$ coupling.

In the reference model, by letting,

$$(\texttt{Zprime : coup2WW}) \sim \left(\frac{M_{Z'}}{M_W}\right)^2 \tag{5.3}$$

[†]In PYTHIA, the width of the Breit-Wigner that describes a resonance is stored in the parameter `id:width`.

we obtain $g_{Z'WW} \sim g_{ZWW}$ leading to a width $\Gamma(Z' \to WW)$ that goes like the fifth power of the Z' mass. For Z' masses of the order of 1 TeV, a process description in terms of a resonance gets compromised due to the rapid grow of the width.
On the other hand, in the extended gauge model we let $(\texttt{Zprime} : \texttt{coup2WW}) \sim 1$, which corresponds to,

$$\frac{g_{Z'WW}}{g_{ZWW}} \sim \left(\frac{M_W}{M_{Z'}}\right)^2 \tag{5.4}$$

giving rise to a width $\Gamma(Z' \to WW)$ that increases linearly with the Z' mass. This was our choice for benchmark model because it allows to study masses at the TeV scale, superseding the reference model prescription.

5.2.2 Kinematic Distributions

The distributions of the Z' resonance peak and its transverse momentum are shown in Fig. 5.6. In the distribution of the Z' mass we observe the width of the peak increasing with $M_{Z'}$. That behavior is expected since the extended gauge model adopted in the simulation imposes a linear increase of $\Gamma(Z' \to WW)$ with the Z' mass.

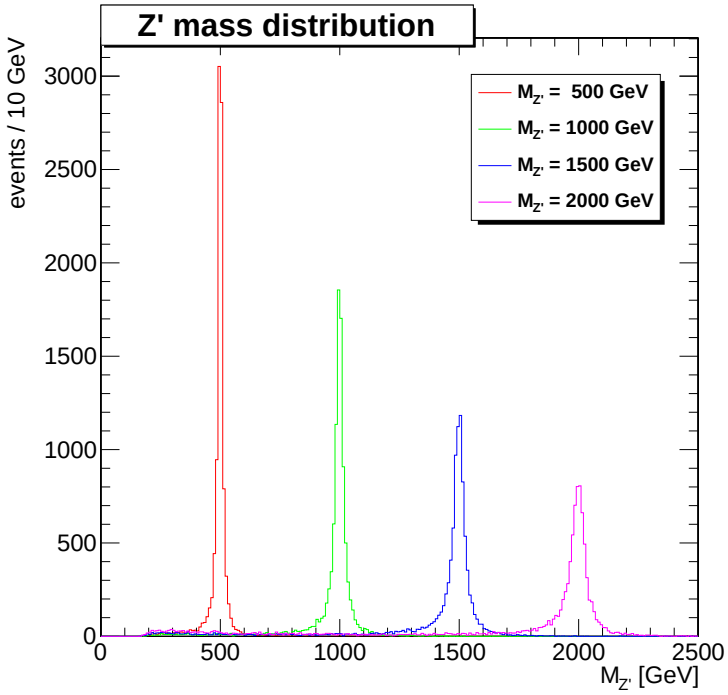

Figure 5.6: Invariant mass distributions of the Z'

Figure 5.7 presents the distributions of the transverse momentum for the W bosons and the Z'. Each W coming from the resonance carries a high p_{T} component while the resonance itself does not, so the Z' is expected to be produced at rest in the laboratory frame. Meanwhile, the p_{T} of each W achieves a maximum near the value $M_{Z'}/2$.

Some kinematic distributions of the final leptons are shown in Fig. 5.8 for electrons and in Fig. 5.9 for muons. Both muons and electrons keep a high p_{T} component from the parent W, with a pseudorapidity distributed around $\eta = 0$. Given the geometry of the muon system of CMS (Fig. 4.5), it is highly possible that the final leptons are within the acceptance region $|\eta| < 2.4$ of the detector.

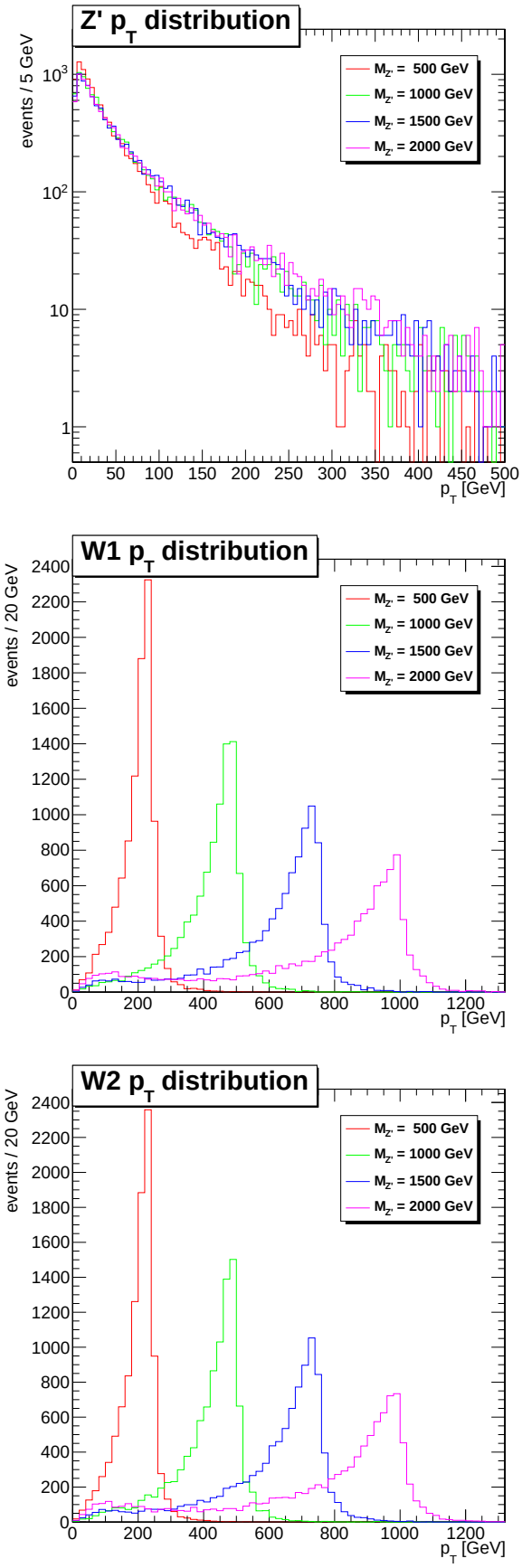

Figure 5.7: Transverse momentum distributions of the Z' and of the W bosons.

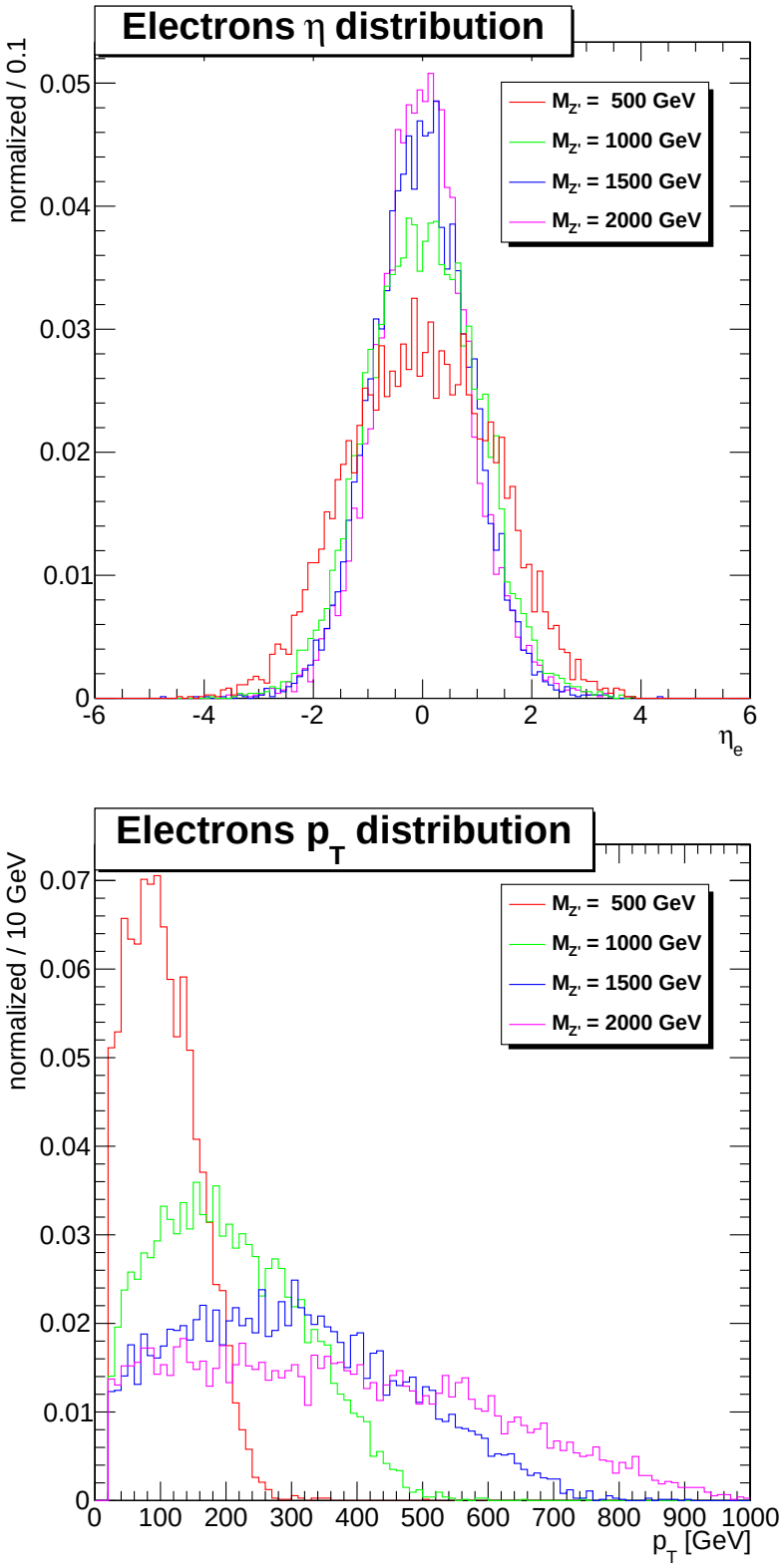

Figure 5.8: Pseudorapidity and transverse momentum distribution of the electrons coming from the *W* bosons.

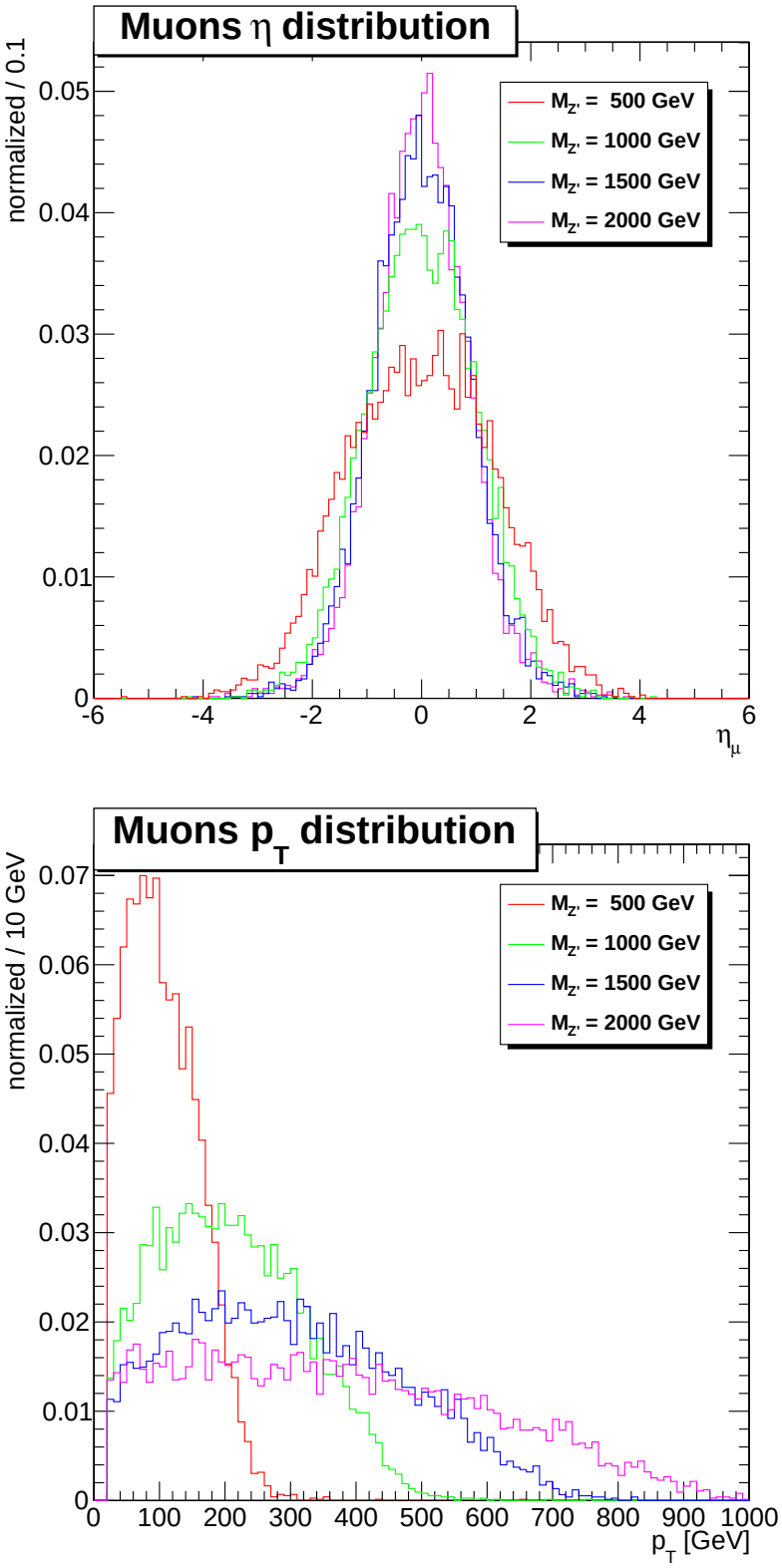

Figure 5.9: Pseudorapidity and transverse momentum distribution of the muons coming from the *W* bosons.

5.3 Background Estimation

In order to estimate the background for the process $pp \to Z' \to W^+W^-$ we have used Monte Carlo datasets from the Summer 2012 season of CMS central production. Initially, some datasets were available in remote locations of the CMS grid, so they were all brought to SPRACE for local analysis.

The processes, generators and cross sections, are given in Table 5.4 together with the Z' samples generated by us with the CMS Fast Simulation tool. The notation indicates the mass of the Z' in TeV, for instance, $Z'_{0.5}$ corresponds to a Z' with mass 0.5 TeV. It can be noticed that the heavier the Z' the smaller the cross section, which in turn is several order of magnitude lower than the major background process involving the top quark ("top").

Process	Dataset name and Generator	Cross section [fb]
top	/TTTo2L2Nu2B_8TeV-powheg-pythia6	2.21×10^4
	/T_tW-channel-DR_TuneZ2star_8TeV-powheg-tauola	1.07×10^4
	/Tbar_tW-channel-DR_TuneZ2star_8TeV-powheg-tauola	1.07×10^4
WW	/WWJetsTo2L2Nu_TuneZ2star_8TeV-madgraph-tauola	4.7×10^3
	/GluGluToWWTo4L_TuneZ2star_8TeV-gg2ww-pythia6	2.3×10^1
WZ	/WZJetsTo2L2Q_TuneZ2star_8TeV-madgraph-tauola	1.7×10^3
	/WZJetsTo3LNu_TuneZ2star_8TeV-madgraph-tauola	8.7×10^2
ZZ	/ZZJetsTo2L2Nu_TuneZ2star_8TeV-madgraph-tauola	2.8×10^2
	/ZZJetsTo2L2Q_TuneZ2star_8TeV-madgraph-tauola	9.1×10^2
	/ZZJetsTo4L_TuneZ2star_8TeV-madgraph-tauola	1.3×10^2
$Z'_{0.5}$	/Zprime05ToWW_8TeV_pythia8	86.9
$Z'_{1.0}$	/Zprime10ToWW_8TeV_pythia8	3.84
$Z'_{1.5}$	/Zprime15ToWW_8TeV_pythia8	4.58×10^{-1}
$Z'_{2.0}$	/Zprime20ToWW_8TeV_pythia8	7.81×10^{-2}

Table 5.4: Monte Carlo datasets used. The LO cross sections come from the generator itself and no uncertainty is provided.

The process "top" includes $t\bar{t}$ production and associate tW, $\bar{t}W$ production. These processes involving a quark t can lead to fully leptonic final states through an intermediate decay $t \to Wb$, which occurs with a fraction [57]

$$\frac{\Gamma(t \to Wb)}{\Gamma(t \to Wb) + \Gamma(t \to Ws) + \Gamma(t \to Wd)} = 0.91 \pm 0.04\,. \tag{5.5}$$

A reaction involving a pair of quark $t\bar{t}$ leading to $1e^+$, $1\mu^-$ and two neutrinos, is depicted in Fig. 5.10. The remaining b quarks may become jets, a signature that could be used to veto this background. The veto on jets has not been implemented during this analysis, but will be added soon.

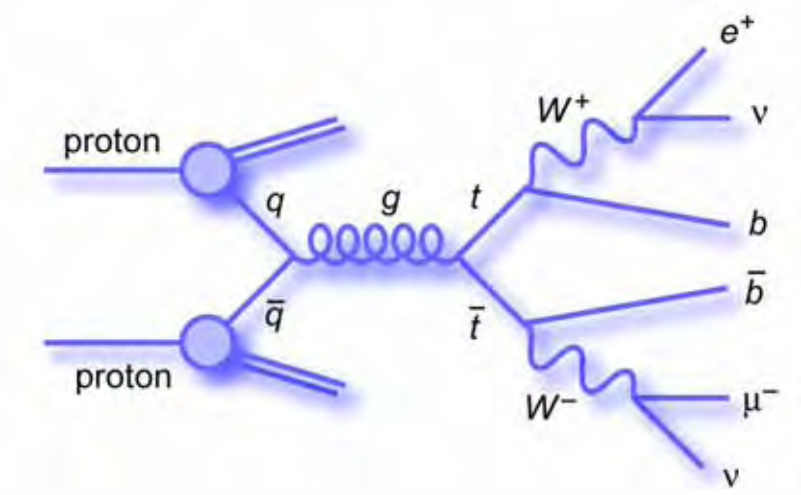

Figure 5.10: Top pair production followed by a W leptonic decay.

Diboson processes WW[‡], WZ and ZZ were also considered as reducible backgrounds. The WW decays were summarized in Table 5.2. The dibosons WZ and ZZ, through the decay mode $Z \to \ell^+\ell^-$ occurring with a fraction $\sim 3\%$, can lead to fully leptonic final states too. As seen in Table 5.4, the diboson processes have cross section lower than the "top" but still higher than any Z' signal.

Single-boson processes, in spite of their large cross section in pp collisions (see Fig. 5.1), are not relevant to our channel since they do not give rise to different flavour leptons plus $\not{E}_{\mathrm{T}}$ in a natural way. We neglected QCD contributions in our background estimation, since the chances of getting high energy leptons coming from this source are very low indeed.

[‡]The notation $WW \equiv W^+W^-$ refers to different-sign pairs, not same-sign pairs.

5.4 Event Selection

We searched for events with a fully leptonic final state consisting of one electron (e), one muon (μ) plus missing transverse energy from undetectable neutrinos, according to the reaction

$$pp \to X \to e\mu \not{E}_{\mathrm{T}} \,. \tag{5.6}$$

Final states with same flavour leptons are rejected, which immediately gets rid of 50% of our signal since both W bosons can decay to same flavour leptons at the generator level. In order to enhance the signal to background ratio, we defined a basic selection proceedure described below:

- At least one primary vertex
- 1μ and $1e$ of opposite charge
- PAT muon, with:

  $p_{\mathrm{T}} > 20$ GeV and $|\eta| < 2.4$

  Identified as PF muon. Global or Tracker muon

  Impact parameter in the transverse plane $d_0 < 0.02$ cm

  Isolation $(calo + track)/p_{\mathrm{T}} < 0.15$

- PAT electron with:

  $p_{\mathrm{T}} > 20$ GeV and $|\eta| < 2.5$

  Ratio of hadronic energy to EM energy: $H/E < 0.05$

  Isolation $(calo + track)/p_{\mathrm{T}} < 0.15$

The selection was made separately for each background sample and then combined. Table 5.5 contains the size of the samples before and after applying the selection requirements, and the number of events normalized to a luminosity $\mathcal{L} = 20\,\mathrm{fb}^{-1}$.

Taking the sample $Z'_{0.5}$ as an example, the selection efficiency is $\varepsilon = 17727/50000 = 0.3545$ which leads to a number of events of

$$n_{Z'} = \sigma \cdot \mathcal{L} \cdot \varepsilon = (86.9\,\mathrm{fb})(20\,\mathrm{fb}^{-1})(0.3545) = 616 \pm 13\,. \tag{5.7}$$

Sample	Generated	Selected	$\sigma \cdot \mathcal{L} \cdot \varepsilon$
top	14.5 M	1.1 M	40,133
WW	2 M	169,000	7,809
WZ	5 M	91,000	819
ZZ	6.6 M	216,000	166
$Z'_{0.5}$	50,000	17,727	616
$Z'_{1.0}$	50,000	21,437	33
$Z'_{1.5}$	50,000	22,175	4.1
$Z'_{2.0}$	50,000	21,647	0.68

Table 5.5: Generated and selected events.

The variance,

$$V(n_{Z'}) = (\sigma \cdot \varepsilon)^2 \cdot V(\mathcal{L}) + (\sigma \cdot \mathcal{L})^2 \cdot V(\varepsilon) = 163 \tag{5.8}$$

was calculated with 2% of relative error on the luminosity,

$$V(\mathcal{L}) \sim (0.02\,\mathcal{L})^2 = 0.16\,\text{fb}^{-2} \tag{5.9}$$

with $V(\varepsilon) \sim (0.002)^2$, and neglected error on the cross section.

It is expected that higher Z' masses lead to lower number of events because the cross section decreases with the mass (see Fig. 5.4). Besides that, the selection efficiency estimated as the ratio Selected/Generated, does not decrease with the mass and reaches a maximum at the sample $Z'_{1.5}$

$$\varepsilon = 22175/50000 = 0.4435\,. \tag{5.10}$$

5.4.1 Selection Efficiency

To estimate the selection efficiency one takes into account the number of events selected m divided by the number generated events, N

$$\varepsilon = \frac{m}{N}\,. \tag{5.11}$$

Since the background contains processes with different cross sections σ_i and

different sizes N_i, one needs to define weights to normalize to a certain integrated luminosity $\mathcal{L}$

$$w_i = \frac{\sigma_i \mathcal{L}}{N_i}\,. \tag{5.12}$$

Before the selection, the effective sample size is given by,

$$N = \sum_i w_i N_i\,. \tag{5.13}$$

The sample size after the selection is,

$$K = \sum_i w_i K_i = \sum_i w_i N_i \varepsilon_i \tag{5.14}$$

where $K_i = N_i\varepsilon_i$ is the i-th sample size after the selection and ε_i is the selection efficiency of the i-th sample. Because all samples are independent, one can estimate the efficiency ε_i for each sample separately. Then, the efficiency for the combined sample corresponds to

$$E = \frac{K}{N} = \frac{\sum_i w_i N_i \varepsilon_i}{\sum_i w_i N_i}\,. \tag{5.15}$$

The asymmetric uncertainty band around E corresponds to the boundaries of a 68.3 % credible region computed in Appendix A. The variance of K can be computed with the usual propagation formula

$$V(K) = \sum_i w_i^2 V(K_i) + V(w_i) K_i^2\,. \tag{5.16}$$

5.4.2 Transverse Invariant Mass

Those events satisfying the basic selection were used to construct a transverse invariant mass M_{T} given by [28],

$$M_{\mathrm{T}} = \left[\left(\sqrt{\left(p_{\mathrm{T}}^{\ell^+\ell'^-}\right)^2 + m^2_{\ell^+\ell'^-}} + \sqrt{\not{E}_{\mathrm{T}}{}^2 + m^2_{\ell^+\ell'^-}}\right)^2 - \left(\overrightarrow{p_{\mathrm{T}}}^{\ell^+\ell'^-} + \overrightarrow{\not{E}}_{\mathrm{T}}\right)^2\right]^{1/2} \tag{5.17}$$

where $\overrightarrow{\not{E}}_{\mathrm{T}}$ is the missing transverse momentum vector, $\overrightarrow{p_{\mathrm{T}}}^{\ell^+\ell'^-}$ is the transverse momentum of the pair $\ell^+\ell'^-$ and $m_{\ell^+\ell'^-}$ is the $\ell^+\ell'^-$ invariant mass.

The resulting M_{T} distribution is shown in Fig. 5.11, with a legend that summarises the signal and background yields normalised to an integrated luminosity of $\mathcal{L} = 20$ fb^{-1}.

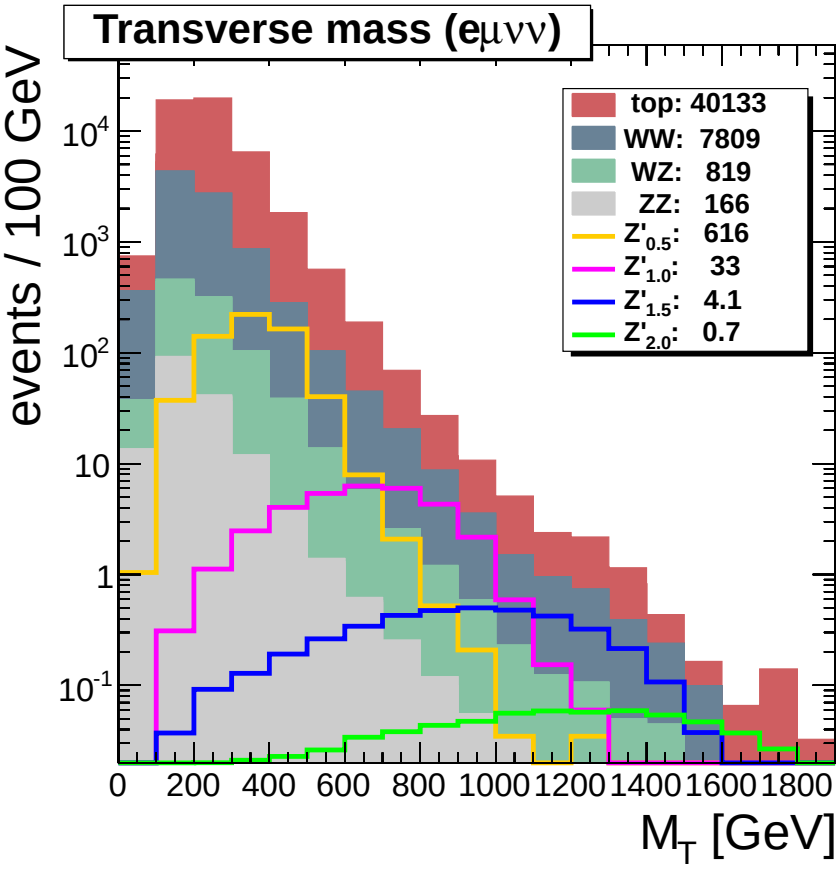

Figure 5.11: Transverse mass distribution normalized to an integrated luminosity $\mathcal{L} = 20$ fb^{-1}. The values in the legend correspond to the ones reported in Table 5.5.

The SM background is represented by the stacked histogram whose area corresponds to 48,927 events made up with 4 contributions

$$\begin{aligned} \text{SM background} = &\quad \text{top} + \text{WW} + \text{WZ} + \text{ZZ} \\ = &\quad 40133 + 7809 + 819 + 166 \,. \end{aligned}$$

Among the considered Z' signals, $Z'_{0.5}$ is the most significant with 616 events

$$\text{Sign. } Z'_{0.5} = \frac{s}{\sqrt{s+b}} = \frac{616}{\sqrt{616+48927}} = 2.77$$

where s and b stand for signal and background, respectively.

The significance gets worse for the higher masses, since

$$\text{Sign. } Z'_{1.0} = \frac{s}{\sqrt{s+b}} = \frac{33}{\sqrt{33+48927}} = 0.15$$

$$\text{Sign. } Z'_{1.5} = \frac{s}{\sqrt{s+b}} = \frac{4.1}{\sqrt{4.1+48927}} = 0.018$$

$$\text{Sign. } Z'_{2.0} = \frac{s}{\sqrt{s+b}} = \frac{0.7}{\sqrt{0.7+48927}} = 0.003$$

5.5 Cut–based Analysis

After the basic selection, a large background still remains, so we must apply further selections. We chose to perform a cut-based analysis in order to improve the significance of the signal. It consists on integrating the M_{T} distribution above a certain threshold chosen to maximise the ratio $s/\sqrt{s+b}$. Let us exemplify the procedure for the $Z'_{0.5}$ case illustrated in Fig. 5.12, where the M_{T} distributions for the signal ($Z'_{0.5}$) and for the background (bkg) are presented.

By adding all the bins above $M_{\mathrm{T}} \geq 300$

$$b = \sum_{M_{\mathrm{T}} \geq 300} \text{bkg} = 9202\,, \qquad s = \sum_{M_{\mathrm{T}} \geq 300} Z'_{0.5} = 437\,.$$

we obtain

$$\text{Sign. } Z'_{0.5}\,(M_{\mathrm{T}} \geq 300) = \frac{s}{\sqrt{s+b}} = \frac{437}{\sqrt{437+9202}} = 4.45$$

We found that the "best cut" corresponds to $M_{\mathrm{T}} \geq 300$ since no other threshold is able to further improve the significance.

The results in Figs. 5.13, 5.14 and 5.15, correspond to the cut-based analysis for the higher masses: $Z'_{1.0}$, $Z'_{1.5}$ and $Z'_{2.0}$, respectively.

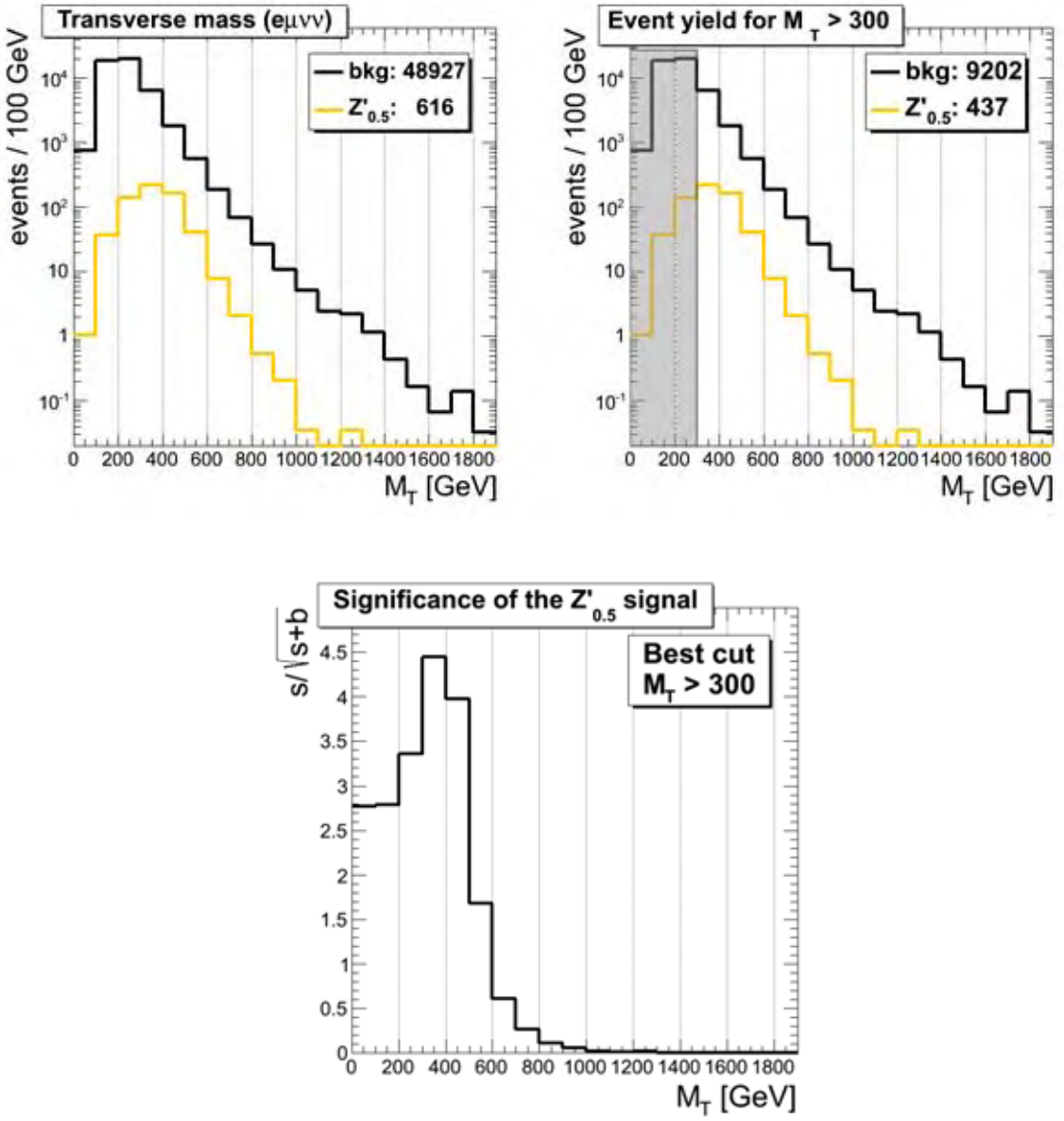

Figure 5.12: Event yield for $M_T > 0$ and $M_T > 300$ (top left and top right), and maximization of the significance for the $Z'_{0.5}$ signal (bottom).

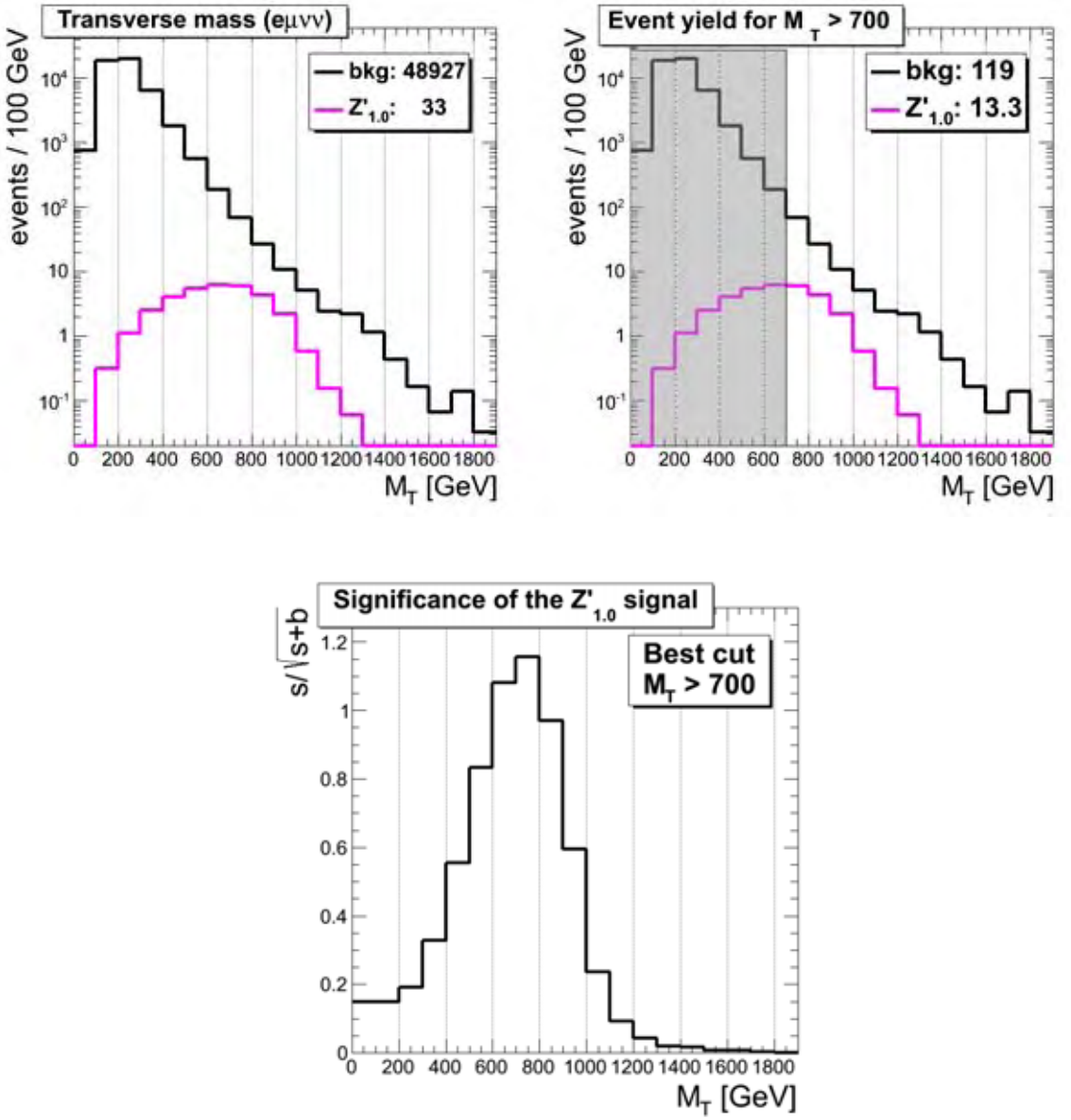

Figure 5.13: Event yield for $M_T > 0$ and $M_T > 700$ (top left and top right), and maximization of the significance for the $Z'_{1.0}$ signal (bottom).

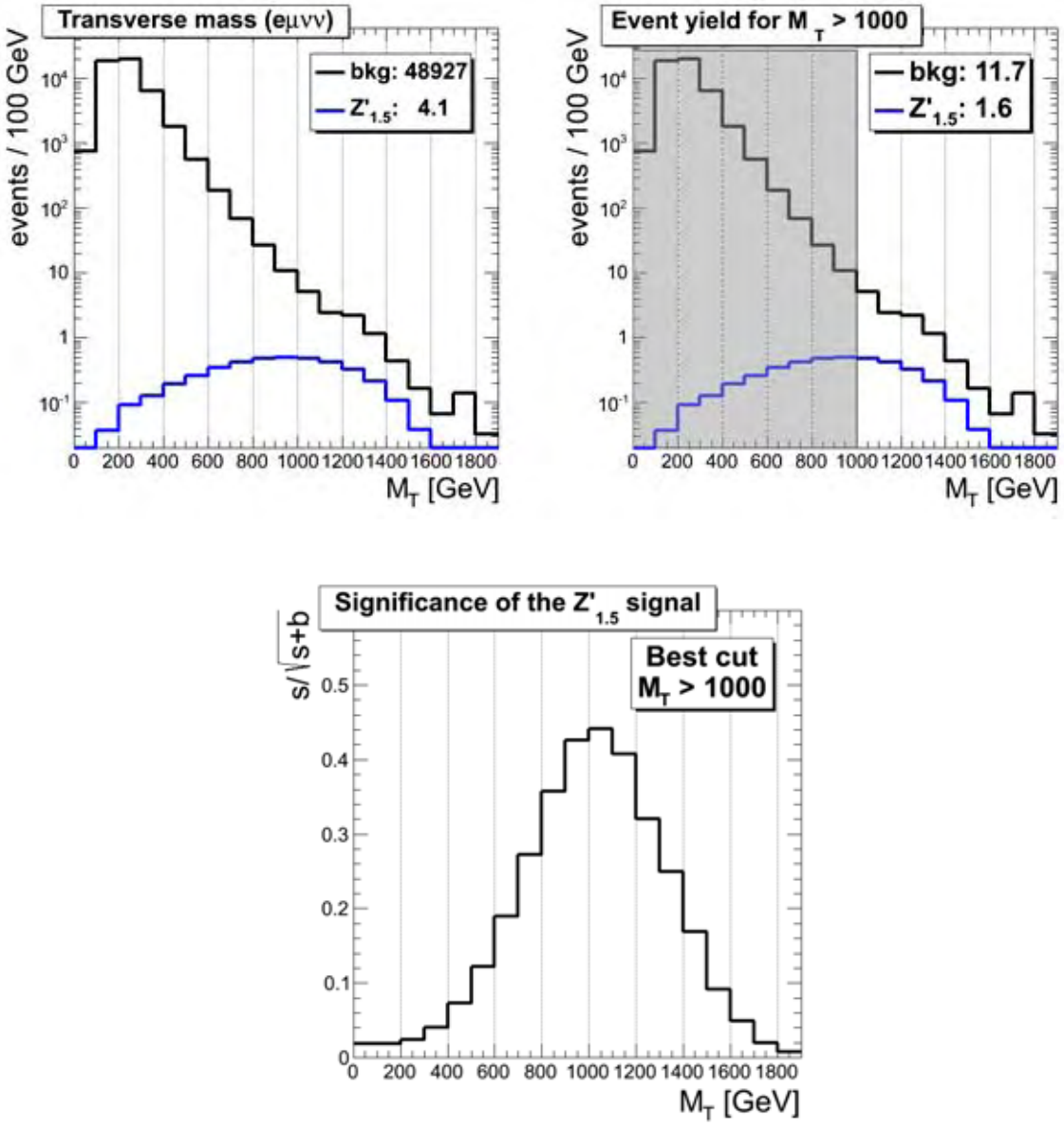

Figure 5.14: Event yield for $M_T > 0$ and $M_T > 1000$ (top left and top right), and maximization of the significance for the $Z'_{1.5}$ signal (bottom).

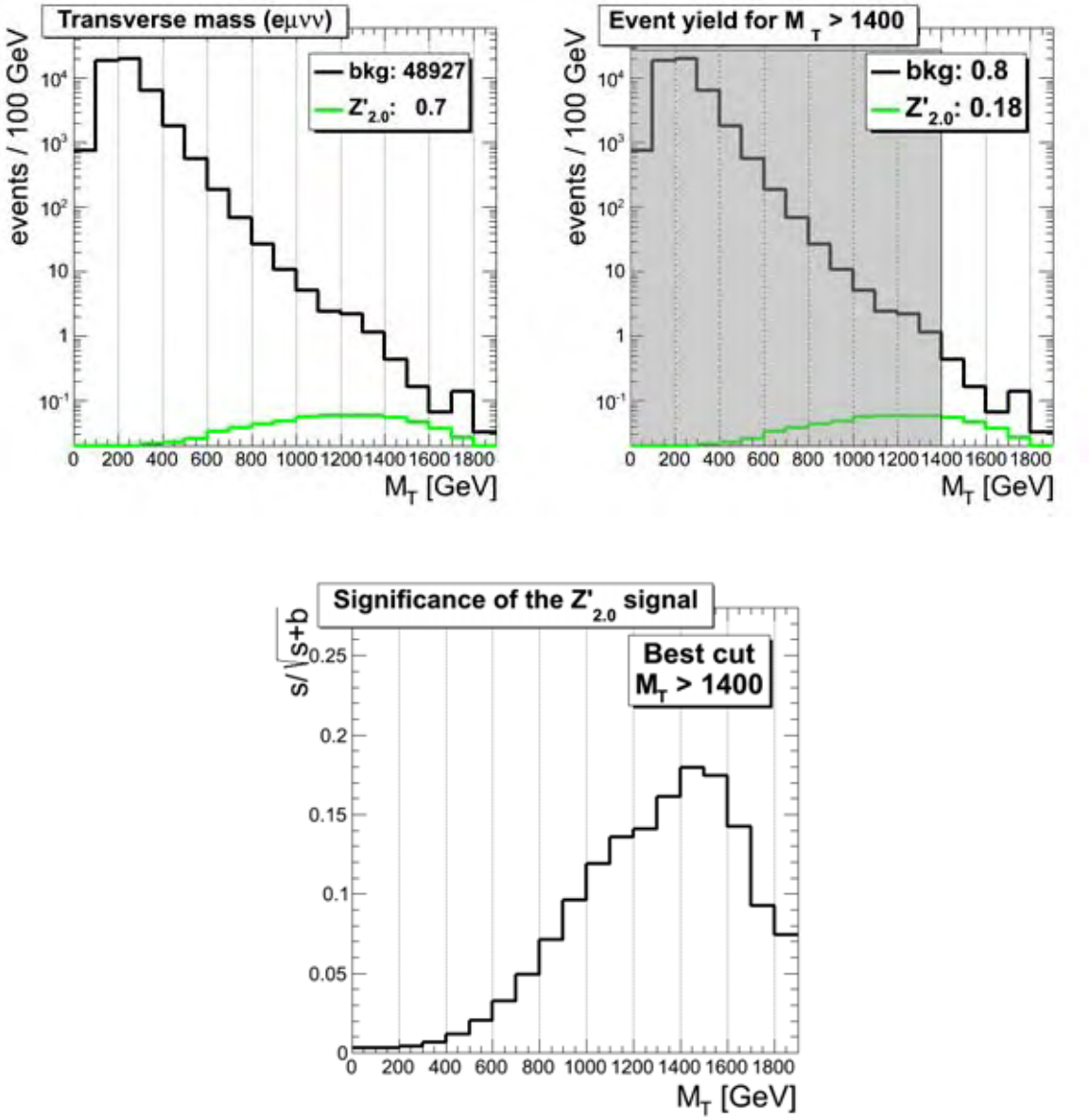

Figure 5.15: Event yield for $M_T > 0$ and $M_T > 1400$ (top left and top right), and maximization of the significance for the $Z'_{2.0}$ signal (bottom).

For each Z' mass, different thresholds were found and they are presented in Table 5.6. It can be noticed that the threshold is always in the region $M_{\mathrm{T}} > M_{Z'}/2$.

$M_{Z'}$ [GeV]	M_{T} [GeV]	Significance
500	300	4.45
1000	700	1.15
1500	1000	0.44
2000	1400	0.18

Table 5.6: Thresholds that maximize the significance.

Adding the cut-based analysis to the basic selection, we increased the significances of the signal and obtained good background rejection, giving an efficiency for the signal that is several orders of magnitude higher than the efficiency for the background, as can be seen in Fig. 5.16.

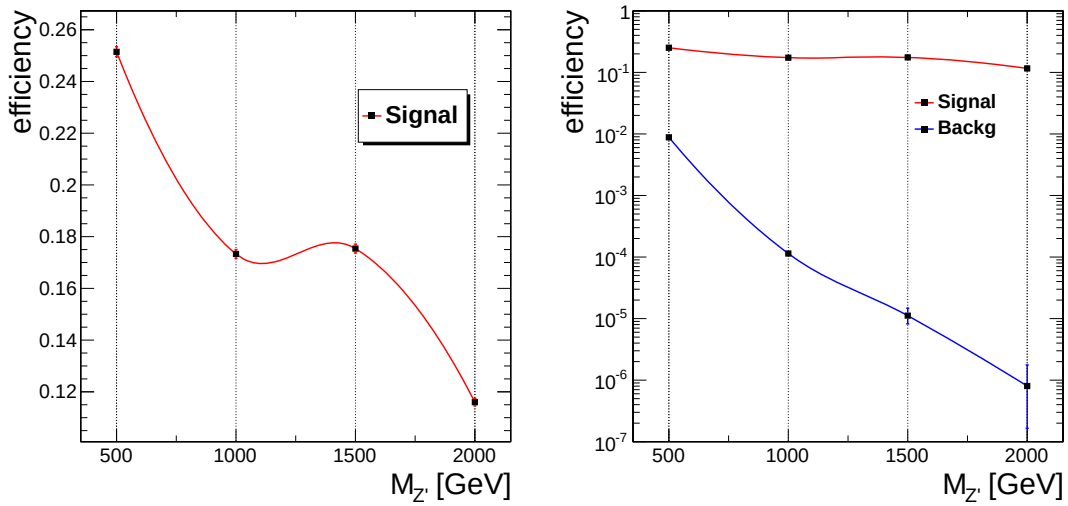

Figure 5.16: Signal (left) and background (right) efficiencies after the full selection.

While in the basic selection the maximum efficiency was obtained for the sample with $M_{Z'} = 1500$ GeV (see Eq. 5.10), after the full selection, the maximum efficiency $\varepsilon = 0.2515 \pm 0.001$ corresponds to the mass $M_{Z'} = 500$ GeV.

For a given Z' mass, the search sensitivity depends on the Z' production cross section times the decay branching ratio into the chosen final state, the signal efficiency, and the level of SM background with the same final state. We can evaluate the sensitivity of our search by calculating the expected limits.

Table 5.7 summarizes the efficiency for the signal and the level of SM background after the full selection.

$M_{Z'}$ [GeV]	$\varepsilon_{Z'}$	SM background	Z' signal
500	0.25	9202 ± 140	437 ± 9
1000	0.17	119 ± 3	13.3 ± 0.3
1500	0.17	11.7 ± 1.2	1.61 ± 0.03
2000	0.12	0.8 ± 0.5	0.181 ± 0.004

Table 5.7: Efficiency of the signal, level of SM background and Z' signal after the full selection. Systematic errors are computed as in Eq. 5.8. Statistical errors are not included.

5.6 Expected Limits

The Confidence Level (CL) quantifies the fraction of times a confidence interval would contain the true value of a parameter in a large number of repeated experiments [60]. The existence or non-existence of an exotic Z' with mass $M_{Z'}$ in a given region is set by the upper limit of a 95% CL interval: if the Z' were actually to exist and have a particular mass, there would be less than 5% probability that statistical fluctuations in the experimental data would have led to that mass.

To focus on a specific case, let us consider the mass $M_{Z'} = 500$ GeV and the respective efficiency of Table 5.7. Assuming the background follows a gaussian (Fig. 5.17) density $p(x)$ with mean $x_0 = 9202$ and standard deviation $\sigma_0 = 140$, the 95% CL expected limit x_{95} is obtained through the integral

$$\int_{x_{95}}^{\infty} p(x)\, dx = 0.05\,. \tag{5.18}$$

The expected limit can be separated in two contributions

$$x_{95} = \underbrace{\sigma \cdot \mathcal{L} \cdot \varepsilon \cdot BR}_{signal} + \underbrace{x_0}_{background} \tag{5.19}$$

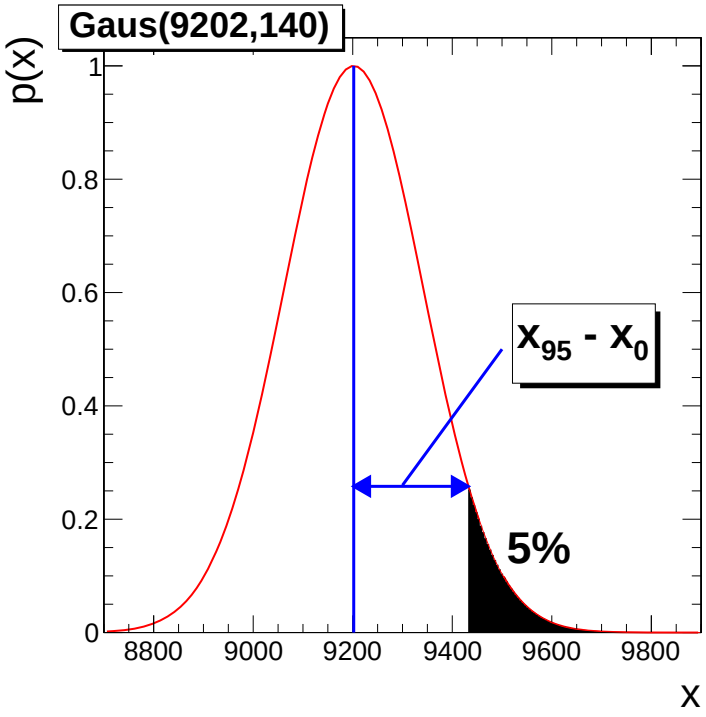

Figure 5.17: Gaussian density. There is less than 5% probability that statistical fluctuations lead a $x > x_{95} = 9432$.

hence, the cross section times branching ration for signal corresponds to

$$\sigma \cdot BR = \frac{x_{95} - x_0}{\mathcal{L} \cdot \varepsilon} = \frac{9432 - 9202}{(20\,\text{fb}^{-1})(0.2515)} = 45.7\,\text{fb}\,. \tag{5.20}$$

The above procedure is very naïve since it does not include the uncertainties. Only the standard deviation of the background was considered to widen the gaussian. To calculate the expected upper limit on the cross section including sistematic uncertainties, a Bayesian method [61] implemented in the macro RooStatsCl95 [62] is recommended by the CMS statistical committee [63].

Inputs to this calculation are:

- Integrated luminosity with its absolute error ($\mathcal{L} = 20 \pm 0.4\,\text{fb}^{-1}$)
- Signal efficiency with its absolute error (column 2 of Table 5.7)
- Level of background with its absolute error (column 3 of Table 5.7).
- Number of pseudo-experiments
- Method: Bayesian with numeric integration

First, the signal efficiency and level of background are assigned priors and modeled via a Monte Carlo method that allows correlation of uncertainties. Then, the expected limit is calculated by simulating pseudo-experiments based on the expected background with Poisson fluctuations.

Figure 5.18 shows the obtained 95% CL upper limit on the signal cross section times branching ratio as a function of the Z' mass. For mass values where the expected limit is above the red line (theoretical) one would not be able to set the existence or non-existence of a Z' for that mass at 95% CL, consequently the search would not be sensitive for that mass.

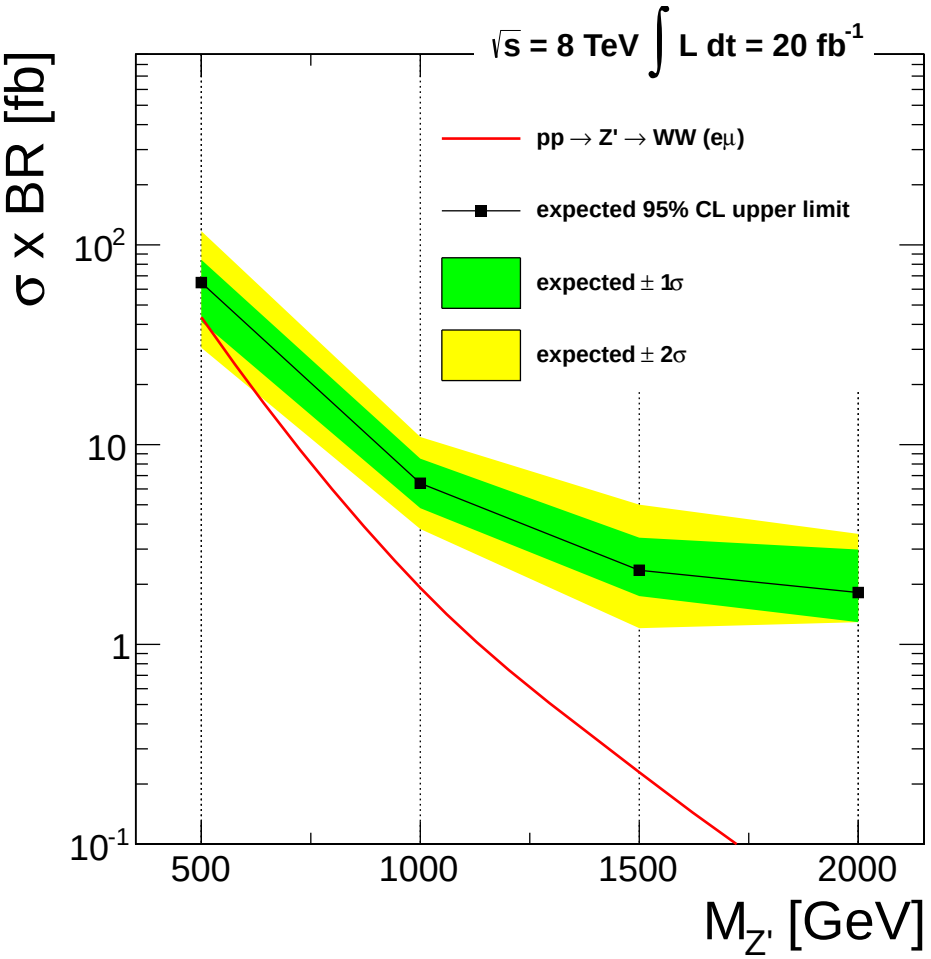

Figure 5.18: Expected upper limit on $\sigma(pp \to Z') \times BR(Z' \to WW \to e\mu \not{E}_{\mathrm{T}})$, with the theoretical prediction at LO (red line). The inner and outer bands represent respectively the 1σ and 2σ uncertainty on the expected limit.

It was not possible to set a 95% CL upper limit on the production of a Z'. The search strategy must be improved to cope with the challenge of searching a Z' coupling to W pairs with a luminosity of just $\mathcal{L} = 20\,\text{fb}^{-1}$. With higher luminosities and the same selection efficiency, our search would be more sensitive. As Fig. 5.19 shows, increasing the luminosity to $\mathcal{L} = 200\,\text{fb}^{-1}$ we could be able to set an upper limit around 1500 GeV.

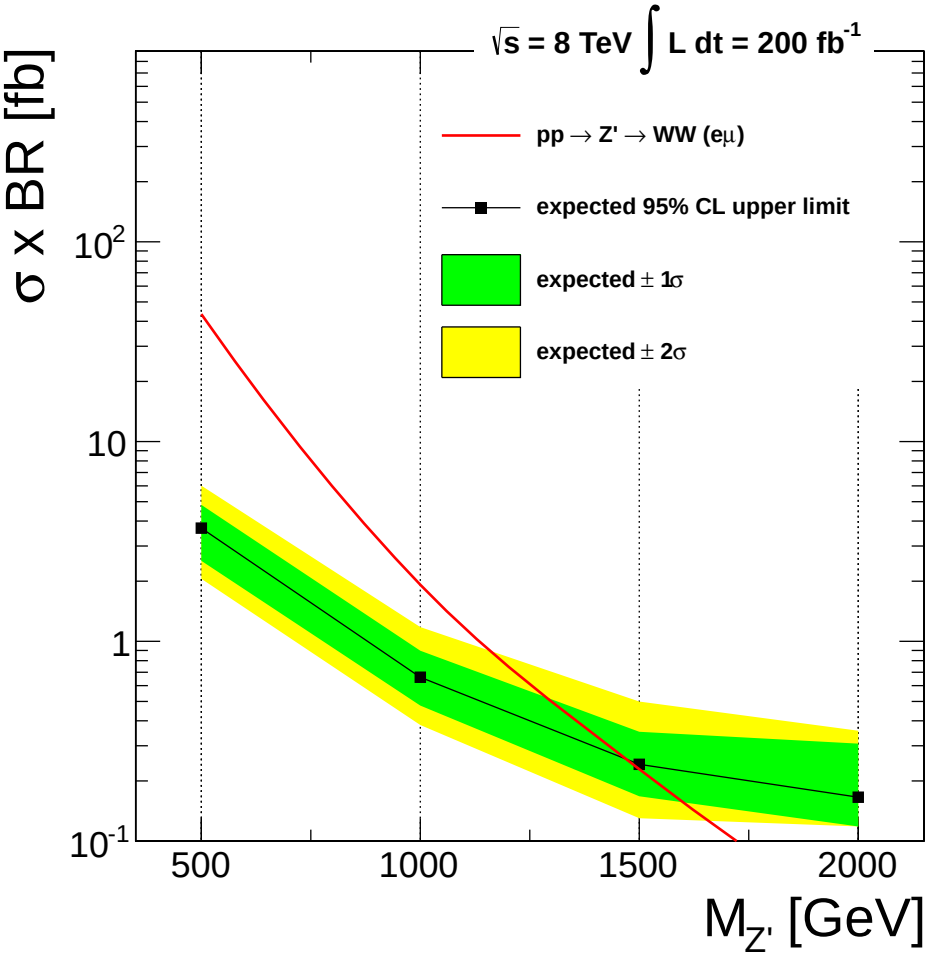

Figure 5.19: Expected upper limit on the cross section with $\mathcal{L} = 200\,\text{fb}^{-1}$.

To establish the existence or non-existence of a Z', we must compare the expected limit, with the observed limit obtained by doing the same analysis upon collision data. As outlook, we intend in the future to compare our simulation with collision data, to optimise the background reconstruction through data-driven methods and to perform a multivariate analysis (MVA) to improve the selection efficiency.

Our expected limit is based upon the study of the transverse mass (Eq. 5.17)

although several quantities like the transverse momentum and pseudorapidity of muons/electrons, the invariant mass of leptons pair, and the missing transverse energy, were looked at separately. Those distributions did not provide better significances than the significance obtained with the variable M_{T}. Nonetheless, the list of variables that can be constructed using MVA methods is endless, and these possibilities must be study to improve the sensibility of the analysis.

Chapter 6

Conclusions

Particle physics is the field that studies the elementary particles and their interactions. The accepted theory to describe the electroweak and strong forces is the standard model (SM). Experiments performed at hadron colliders support the SM, although a plethora of theories have been trying to supersede.

The study of the electroweak symmetry breaking sector is one of the main goal of the LHC experiments. Unitarity arguments based on vector boson scattering suggests the existence of a light Higgs responsible for avoiding the unphysical growth of the scattering amplitude. This scenario seems to be true after the discovery of the 125 GeV boson that resembles in many ways the scalar Higgs boson from the minimal Standard Model.

However, it has been proposed in the last decades several alternative approaches to this minimal implementation of the symmetry breaking. Some of these scenarios beyond the standard model motivate the existence of new heavy neutral resonances that can be detected by their decay into a pair of W bosons. Consequently, the diboson W^+W^- fully leptonic channel was chosen because this mode yields cleaner spectra, in comparison with hadronic channels involving jets.

The outstanding performance of the Large Hadron Collider (LHC) over the first three years of operation has allowed to collect more data than any previous hadronic experiment. The observation of a candidate to Higgs boson both by CMS and Atlas, the realisation of precision measurements, and the improvement of limits for a variety of models beyond SM, are some of the CERN achievements in the LHC era.

This study presented here is based on a simulation of the CMS detector considering the operation parameters of the LHC during the 2012 proton-proton run, *i.e.*, center-of-mass energy of 8 TeV and integrated luminosity of 20 fb $^{-1}$. The diboson fully leptonic channel allows the reconstruction of the W^+W^- transverse mass through the detection of leptons and missing transverse energy.

We use PYTHIA together with the CMS FastSim to produce samples of a hypothetical Z' heavier than the standard Z boson. We evaluate the sensitivity to observe the signal of the Z' over the SM background, considering four different benchmark values of the mass: $M_{Z'}$ = 0.5, 1, 1.5, and 2 TeV. In order to improve the significance of the signal, a cut and count analysis was performed by optimising the ratio $s/\sqrt{s+b}$.

The resulting signal efficiency and level of SM background allowed us to calculate the 95% expected limits on the cross section times branching ratio

$$\sigma(pp \to Z') \times BR(Z' \to WW \to e\mu \not{E}_{\mathrm{T}}) \; .$$

By comparing the expected limit with the theoretical value, we find the former greater. This means that the cross section of the signal is very low and our selection procedure is not enough to observe a significant excess upon the number of events dominated by the SM background. We conclude that our adopted channel lacks sensitive to search Z' resonances in the mass range $[500,\ 2000]$ GeV. Increasing the luminosities to $\mathcal{L} = 200\,\mathrm{fb}^{-1}$ and keeping the same selection criteria, the channel becomes more sensitive being able to exclude masses below $\sim$1500 GeV.

The main purpose of a search for physics beyond the SM is to reduce the parameter space left by the model under study. To accomplished this task one must compare expected with observed limits, and this requires the analysis of both Monte Carlo and collision data. As outlook, the comparison between our simulation and data recorded by CMS during 2012 has to be done. The analysis can be optimised using data-driven methods for background reconstruction, and the sensitivity can be improved by introducing multivariate analysis techniques which allow a more efficient selection.

Finally, the channels $WW \to e\mu \not{E}_{\mathrm{T}}$, $WW \to ee \not{E}_{\mathrm{T}}$, and $WW \to \mu\mu \not{E}_{\mathrm{T}}$, can be added to get more stringent limits. Such combination would increase the sensitivity to rule out signals with low cross section like the Z' hypotheses simulated in this work.

Appendix A

Statistical Uncertainty for Efficiency

The usual approach when estimating a selection efficiency is to treat the number of selected events m as a binomially distributed variable, *i.e.*, one finds m "successes" out of N independent trials, where the probability of success on each trial is the efficiency ε. That is, the probability to select m events is

$$P(m; N, \varepsilon) = \frac{N!}{m!(N-m)!}\varepsilon^m(1-\varepsilon)^{N-m}\,. \tag{A.1}$$

The log-likelihood function for the unknown parameter ε is

$$\ln \mathcal{L}(\varepsilon) = m \ln \varepsilon + (N-m)\ln(1-\varepsilon) + C \tag{A.2}$$

where C represents terms that do not depend on ε and can therefore be dropped. Setting the derivative of $\ln \mathcal{L}(\varepsilon)$ equal to zero gives

$$\hat{\varepsilon} = \frac{m}{N} \tag{A.3}$$

where the hat is used to denote the estimator of the true parameter ε.

It has been recommended [64] the class TEfficiency available in ROOT [44] to get the variance of the estimator $\hat{\varepsilon}$. We employed the method TEfficiency::Bayesian to get 68% CL credible intervals $[\varepsilon_{\text{lo}}, \varepsilon_{\text{up}}]$, where

$$\varepsilon_{\text{up/lo}} = \text{TEfficiency::Bayesian}\,(N,\, m,\, 0.683,\, \alpha,\, \beta,\, \text{true/false})$$

are the upper and lower limits of the interval, respectively. ROOT supports beta distributions with two free parameters (α, β) as prior probabilities. In bayesian statistics [61] a likehood-function (how probable is it to get the observed data assuming a true efficiency) and a prior probability (what is the probability that a certain true efficiency is actually realized) are used to determine the posterior probability by using Bayes theorem.

Bibliography

[1] G. t Hooft, "Gauge theories of the forces between elementary particles", *Scientific American* 242 6, 104-138 (1980)

[2] Miscellaneous Pictures in Physics, http://www.staff.science.uu.nl/∼hooft101/lectures/pictures.html

[3] S. Novaes, "Standard Model: An Introduction", published in "Particle and Fields", Proceedings of the 10th Jorge Andre Swieca Summer School, (World Scientific, Singapore) (2000), arXiv:hep-ph/0001283

[4] C. Quigg, "Gauge Theories of the Strong, Weak and Electromagnetic Interactions", first edition (1984); reprinted, Advanced Book Classic (1997)

[5] P. Langacker, "The Physics of Heavy Z' Gauge Bosons", *Rev. Mod. Phys.* 81, 1199-1228 (2008), arXiv:0801.1345v3

[6] C. Quigg, "Unanswered Questions in the Electroweak Theory", *Ann. Rev. Nucl. Part. Sci.* 59, 505-555 (2009), arXiv:0905.3187v2

[7] S. P. Martin, "A Supersymmetry Primer', sixth edition (2011), arXiv:hep-ph/9709356v6

[8] B.C. Allanach, et. al., "Les Houches Physics at TeV Colliders 2005. Beyond the Standard Model working group: summary report" (2005), arXiv:hep-ph/0602198

[9] M. Bustamante, L. Cieri, and J. Ellis, "Beyond the Standard Model for Montaneros", Lectures by John Ellis at the 5th CERN-Latin-American School of High-Energy Physics, Recinto Quirama, Colombia, *CERN-PH-TH-2009-223* (2009)

[10] N. Arkani-Hamed, A. G. Cohen, H. Georgi, "Electroweak symmetry breaking from dimensional deconstruction", *Phys. Lett.* B 513, 232-240 (2001)

[11] C. Csaki, "TASI Lectures on Extra Dimensions and Branes", Lectures at the Theoretical Advanced Study Institute, University of Colorado (2002), arXiv:hep-ph/0404096

[12] K. Dienes, "New Directions for new Dimensions: An Introduction to Kaluza-Klein Theory, Large Extra Dimensions, and the Brane World", TASI Lectures (2002)

[13] L. Randall, R. Sundrum, "Large Mass Hierarchy from a Small Extra Dimension", *Phys. Rev. Lett.* 83, 33703373 (1999)

[14] T.R.F.P. Tomei, "Busca por dimensões extras no Detector CMS do Large Hadron Collider", Tese de doutoramento, IFT-UNESP (2012)

[15] A. Santos, "Procura de Sinais de Dimensões Extras Universais em Colisões Próton Antipróton", Tese de doutoramento, IFT-UNESP (2012)

[16] F. Dias, "Busca por Ressonâncias de Grávitons em Modelos com Dimensões Extras no LHC", Tese de doutoramento, IFT-UNESP (2012)

[17] C. Bernardes, "Busca por Dimensões Extras Universais no Detector CMS do LHC", Dissertação de mestrado, UFABC (2012)

[18] J. Beringer et al. (PDG), "Grand Unified Theories", *Phys. Rev.* D 86, 010001 (2012)

[19] H. Georgi, S. Glashow, "Unity of All Elementary-Particle Forces", *Phys. Rev. Lett.* 32, 438 (1974)

[20] H. Fritzsch, P. Minkowski, "Unified interactions of leptons and hadrons", *Annals Phys.* 93, 193-266 (1975)

[21] J. Hewett, T. Rizzo, "Low-Energy Phenomenology of Superstring Inspired E(6) Models", *Phys. Rept.* 183, 193 (1989)

[22] The URL of the Fermilab, http://www.fnal.gov/

[23] CMS Collaboration, "CMS Exotica Public Physics Results", https://twiki.cern.ch/twiki/bin/view/CMSPublic/PhysicsResultsEXO

[24] ATLAS Collaboration, "ATLAS Experiment Exotic Public Results", https://twiki.cern.ch/twiki/bin/view/AtlasPublic/ExoticsPublicResults

[25] CMS Collaboration, "Search for Resonances in Dilepton Mass Spectra in pp Collisions at $\sqrt{s}$ = 8 TeV", *CMS Physics Analysis Summary* EXO-12-061 (2013)

[26] ATLAS Collaboration, "Search for high-mass dilepton resonances in 20 fb^{-1} of pp collisions at $\sqrt{s}$ = 8 TeV with the ATLAS experiment", *ATLAS Note* ATLAS-CONF-2013-017 (2013)

[27] B. Lee, C. Quigg, H. Thacker, "Weak interactions at very high energies: The role of the Higgs-boson mass", *Phys. Rev.* D 16, 5 (1977)

[28] O. Éboli et al. "Signals for New Spin-1 Resonances in Electroweak Gauge Boson Pair Production at the LHC", *Phys. Rev.* D 80, 073011 (2009)

[29] O. Éboli et al. "Present Bounds on New Neutral Vector Resonances from Electroweak Gauge Boson Pair Production at the LHC ", *Phys. Rev.* D 85, 055019 (2012)

[30] J. Gonzalez-Fraile, "Update of the Present Bounds on New Neutral Vector Resonances from Electroweak Gauge Boson Pair Production at the LHC", Presented at Phenomenology 2012 Symposium (2012), arXiv:1205.5802

[31] CERN's accelerator complex, http://user.web.cern.ch/public/en/research/AccelComplex-en.html

[32] LHC Design Report VOL. I and VOL. II, http://lhc.web.cern.ch/lhc/LHC-DesignReport.html

[33] Public CMS Luminosity Information, https://twiki.cern.ch/twiki/bin/view/CMSPublic/LumiPublicResults

[34] The URL of the CMS Collaboration, http://cms.cern.ch

[35] CMS Collaboration, http://cms.web.cern.ch/tags/cms-detector

[36] CMS Collaboration, "Missing Transverse Energy Performance in Minimum-Bias and Jet Events from Proton-Proton Collisions at $\sqrt{s}$ = 7 TeV", *CMS Physics Analysis Summary*, JME-10-004 (2010)

[37] CMS Collaboration, "Particle-Flow Event Reconstruction in CMS", *CMS Physics Analysis Summary*, PFT-09-001 (2009)

[38] C. Lippmann, "Particle identification", *Nuclear Instruments and Methods in Physics Research* A 666 148-172 (2012)

[39] V. Khachatryan et al., "CMS Tracking Performance Results from early LHC Operation", *European Physical Journal* C 70 1165-1192 (2010)

[40] J. Beringer et al. (PDG), "Monte Carlo Event Generators", *Phys. Rev.* D 86, 010001 (2012)

[41] T. Sjöstrand, "PYTHIA Documentation", http://home.thep.lu.se/∼torbjorn/Pythia.html

[42] M.L. Mangano et al.,"ALPGEN: a generator for hard multiparton processes in hadronic collisions", *JHEP* 07 001 (2003)

[43] F. Maltoni, T. Stelzer, "MadEvent: Automatic Event Generation with MadGraph", *JHEP* 02 027 (2003)

[44] R. Brun, F. Rademakers, "ROOT - An Object Oriented Data Analysis Framework", *Meth. in Phys. Res.* A 389 81-86, http://root.cern.ch/ (1997)

[45] CMS Collaboration, "CMS Electroweak Public Physics Results", https://twiki.cern.ch/twiki/bin/view/CMSPublic/PhysicsResultsEWK

[46] CMS Collaboration, "Measurement of the W^+W^- and ZZ production cross sections in pp Collisions at $\sqrt{s}$ = 8 TeV", CMS-SMP-12-024, CERN-PH-EP-2012-376, arXiv:1301.4698 (2012)

[47] K. Agashe, H. Davoudiasl, G. Perez, and A. Soni, "Warped Gravitons at the LHC and Beyond", *Phys. Rev.* D 76, 036006 (2007)

[48] J. Beringer et al. (PDG), "$W^+ Decay Modes$", *Phys. Rev.* D 86, 010001 (2012)

[49] T. Aaltonen et al. (CDF Collaboration), "Search for WW and WZ Resonances Decaying to Electron, Missing E_T, and Two Jets in $p\bar{p}$ Collisions at $\sqrt{s} = 1.96$ TeV", *Phys. Rev. Lett.* 104, 241801 (2010)

[50] V. M. Abazov et al. (DØ Collaboration), "Search for Resonant WW and WZ Production in $p\bar{p}$ Collisions at $\sqrt{s} = 1.96$ TeV", *Phys. Rev. Lett.* 107, 011801 (2011)

[51] CMS Collaboration, "Search for heavy resonances in the W/Z-tagged dijet mass spectrum final state in pp collisions at 7 TeV", CMS-EXO-11-095, CERN-PH-EP-2012-356 (2012)

[52] ATLAS Collaboration, "Search for new phenomena in the $WW \to \ell\nu\ell'\nu'$ final state in pp collisions at sqrt(s) = 7 TeV with the ATLAS detector", ATLAS-CONF-2012-068, ATLAS-COM-CONF-2012-119 (2012)

[53] CMS Collaboration, "Fast Simulation Offline Guide", https://twiki.cern.ch/twiki/bin/view/CMSPublic/SWGuideFastSimulation

[54] S. Agostinelli et al., "Geant4 – a simulation toolkit", *Nuclear Instruments and Methods in Physics Research* A 506, 250-303 (2003)

[55] CMS Collaboration, "Physics Analysis Toolkit", https://twiki.cern.ch/twiki/bin/view/CMSPublic/WorkBookPAT

[56] CMS Collaboration, "The CMS Offline WorkBook", https://twiki.cern.ch/twiki/bin/view/CMSPublic/WorkBook

[57] J. Beringer et al. (PDG), "Quarks Summary Table", *Phys. Rev.* D 86, 010001 (2012)

[58] J. Beringer et al. (PDG), "Mass Limits of Z' (Heavy Neutral Vector Boson Other Than Z)", *Phys. Rev.* D 86, 010001 (2012)

[59] G. Altarelli, B. Mele and M. Ruiz-Altaba, "Searching for new heavy vector bosons in $p\bar{p}$ colliders", *Z. Phys.* C 45, 109-121 (1989)

[60] G. Cowan, "Statistical Data Analysis", Oxford (1995)

[61] J. Heinrich et al., "Interval estimation in the presence of nuisance parameters. 1. Bayesian approach", CDF7117 (2004), arXiv:0409129

[62] CMS Collaboration, "RooStatsCl95: Upper Limit Calculator for a Counting Experiment", https://twiki.cern.ch/twiki/bin/view/CMS/RooStatsCl95

[63] CMS Statistics Committee,
https://twiki.cern.ch/twiki/bin/view/CMS/StatisticsCommittee

[64] D. Casadei, "Estimating the selection efficiency", *JINST* 7, P08021 (2012), arXiv:0908.0130v8